The rheological evolution of a phonotephritic melt upon variable degrees of carbonate assimilation and deformation regimes

Gabriele Giuliani[1*], Danilo Di Genova[2], Fabrizio Di Fiore[3], Silvio Mollo[3,4], Serena Dominijanni[5], Chiara Maria Petrone[6], Claudia Romano[1], Alessandro Vona[1]

[1] Dipartimento di Scienze, University of Roma Tre, L.go San Leonardo Murialdo 1, 00146 Roma, Italy
[2] Institute of Science, Technology and Sustainability for Ceramics (ISSMC), National Research Council of Italy (CNR), Italy
[3] National Institute of Geophysics and Volcanology, Section of Roma 1, Via di Vigna Murata 605, 00143 Roma, Italy
[4] Department of Earth Sciences, Sapienza – University of Rome, P. le Aldo Moro 5, 00185 Roma, Italy
[5] Institute of environmental geology and geoengineering (IGAG), National Research Council of Italy (CNR), Italy
[6] Natural History Museum, Volcano Petrology Group, Cromwell Road, SW7 5BD London, UK

*Corresponding author (gabriele.giuliani@uniroma3.it)

Abstract

The dynamic interplay between magmas and carbonate wall rocks within volcanic plumbing systems heavily influences the chemical and physical properties of erupted magmas. In this study we present results from isothermal static experiments (ISEs) and isothermal deformation experiments (IDEs) aimed at investigating the rheological evolution of a phonotephritic melt from Somma-Vesuvius (Italy) under variable shear rates and CaO and CaO+MgO doping levels. Flash differential scanning calorimetry is also used to determine the viscosity of interstitial melt, allowing for the first direct assessment of how crystallization affects melt rheology without relying on empirical viscosity models. Two distinct rheological scenarios emerge from IDEs: 1) a viscous deformation, characterized by uniform flow, and 2) a non-homogeneous deformation, featuring shear localization and viscous/brittle rupture of the magma. As both shear rate and doping level increase, a non-Newtonian melt behavior is observed due to stress localization and rupture, facilitated by the development of the crystal network. The narrower viscosity range measured from IDEs, compared to models of pure viscous behavior, suggests that shear localization and fracturing reduce the resistance to flow in doped, crystal-rich samples. The complex rheology of doped melts reflects the disaggregation of skarn shells at the margins of magma chambers, thereby facilitating skarn recycling and enhancing magma contamination.

Keywords: melt rheology, shear rate, magma-carbonate assimilation, skarn rocks

1. Introduction

The interaction between magmas and surrounding country rocks is a dynamic process that occurs under various volcanic settings and across different timescales (e.g., Huber et al., 2009; Sparks et al., 2019; Knuever et al., 2023a). When magma stalls within the carbonate crust its interaction with the country rock involves mechanical, thermal, and chemical processes, including convective flux/strain rate, thermal cracking, heat loss/exchange between the hot magma and the cold carbonate, and contamination phenomena (Caricchi et al., 2021; Del Gaudio and Ventura, 2008; Di Rocco et al., 2012; Mollo et al., 2010; Mollo and Vona, 2014). These processes promote the erosion and transport of host rock portions and metamorphosed blocks into the magmatic body, while heat loss/exchange results in decarbonation reactions at the magma-carbonate interface (Knuever et al., 2023b). However, limestone and dolostone decarbonation reactions promote the assimilation of CaO and CaO+MgO by magma, thereby changing the chemistry of the parental melt and ultimately influencing its rheology. At the same time, the intricate multi-step progression from the interior of the magma chamber to the carbonate wall rock facilitates the formation of different skarn rocks, which are categorized as 1) exoskarns, forming through solid-state thermal metamorphic reactions in the carbonate protolith, and 2) endoskarns, crystallizing directly from magmas that assimilate carbonate materials (Barnes et al., 2005; Carter and Dasgupta, 2016; Di Rocco et al., 2012; Knuever et al., 2023b; Mollo and Vona, 2014; Wenzel et al., 2002).

At Somma-Vesuvius (Italy), the assimilation of carbonate by magmas is testified by the presence in the erupted products of abundant exoskarn/endoskarn xenoliths, reflecting various degrees of CaO and MgO contamination at shallow depths within the magma chamber (Bruno et al., 1998; Jolis et al., 2015). Somma-Vesuvius is characterized by different types of eruptions, ranging from effusive lava flows to explosive Strombolian, sub-plinian and plinian events, with compositions variable from mildly silica-undersaturated (basalt to trachyte) to highly silica-undersaturated (tephrite to phonolite). This variability in eruptive/compositional styles is attributed to changes in the mantle source (Ayuso et al., 1998; Peccerillo, 2019, 2001; Somma et al., 2001), magma mixing and differentiation (Cioni et al., 1995; Civetta et al., 1991), and magma-carbonate interaction (Del Moro et al., 2001; Gilg et al., 2001).

To date, several experimental studies across various volcanic settings have underscored the impact of mechanical deformation on the crystallization kinetics, which influences the rheological evolution of the melt, the transport capability of magma and its eruptive style (Chevrel et al., 2015; Di Fiore et al., 2024, 2021a;

Harris et al., 2020; Kolzenburg et al., 2022, 2018, 2016; Mollo et al., 2020; Vetere et al., 2021, 2024; Vetere and Holtz, 2020; Vona et al., 2011; Vona and Romano, 2013). One of the primary effects of the deformation regime on melt crystallization is the reduction of the activation energy for nucleation, which is achieved by increasing the likelihood of random collisions of atoms within the melt phase (Hammer, 2008; Kolzenburg et al., 2018; Kouchi et al., 1986; Tripoli et al., 2019). Because the diffusive atomic mobility increases upon the effect of convective stirring, the crystallization rate of the melt markedly increases as the result of a shorter incubation time of nucleation (Di Fiore et al., 2022; Hammer, 2008; Kouchi et al., 1986; Sehlke et al., 2014; Vetere et al., 2021; Vona and Romano, 2013).

To elucidate the impact of dynamic deformation on the rheological evolution of magmas upon crystallization, two interrelated effects must be considered: (1) the crystallinity change resulting from an enhanced crystal nucleation and growth process, and (2) the compositional evolution of the residual melt as a function of crystallization (Di Fiore et al., 2023, 2021b; Kolzenburg et al., 2018, 2016; Picard et al., 2013; Sehlke et al., 2014; Sehlke and Whittington, 2020; Soldati et al., 2024). The physical influence of particles on viscosity has been the subject of extensive investigation, prompting substantial efforts aimed at developing, validating, and parameterizing models that describe the rheology of multiphase suspensions (Costa et al., 2009; Frontoni et al., 2022; Mader et al., 2013; Pabst et al., 2006; Vona et al., 2011). Suspended solid particles are rigid obstacles in a flow which increase viscous dissipation by forcing the fluid flow lines to deviate around them. Whilst particles may accommodate some of the bulk strain in the suspension through solid-body rotation, the viscosity of a particle suspension is always higher than the viscosity of the particle-free liquid (Mader et al., 2013; Mueller et al., 2010). As the solid fraction in a suspension increases, a significant shift occurs in response to a transition towards solid-like behavior. This critical point, defined by the maximum packing density of the particles, marks the threshold where fluid flow ceases, and the system may undergo brittle failure under additional stress. The evolution through distinct rheological states is influenced not only by particle concentration but also by factors such as particle shape, size, distribution, and orientation (Arzilli et al., 2022, 2019; Kolzenburg et al., 2020; Lejeune and Richet, 1995; Moitra and Gonnermann, 2015; Mueller et al., 2010; Pabst et al., 2006; Pistone et al., 2016; Vona et al., 2011).

Building upon the above considerations, Giuliani et al. (2024) conducted a systematic study with the aim to investigate the influence of CaO and Cao+MgO on the crystal-free rheological evolution of a

phonotephrite melt from Somma-Vesuvius, under both high- and low-temperature regimes. The composition of the CaO and CaO+MgO-doped starting material closely resembled that of melt inclusions and interstitial glasses found in natural skarn xenoliths due to assimilation of carbonate rocks by magmas. Giuliani et al (2024) found that the pristine melt exhibits the highest viscosity above a critical temperature of 750 °C, while attaining the lowest viscosity values below this threshold. The addition of CaO resulted in a significantly larger variation in viscosity compared to the combined addition of CaO+MgO, highlighting the dominant role of CaO over MgO in modifying the viscosity of the silicate liquid.

Here we experimentally investigate how the deformation regime and carbonate assimilation collectively affect the crystallization and multiphase rheology of the same phonotephritic melt from Somma-Vesuvius. Using flash differential scanning calorimetry, we extracted the viscosity of the residual melt, enabling, for the first time, a precise assessment of crystallization effects on melt rheology without relying on empirical viscosity models. We have recently documented that these models perform poorly within the chemical parameters of this study (Giuliani et al., 2024). By examining the interaction between mechanical deformation and melt contamination, we explore the processes governing the nucleation and growth of crystals, along with the resulting changes in the melt viscosity. Our contribution provides insights into the mechanisms that control the efficiency of magma transport in volcanic systems open to variable degrees of carbonate assimilation.

2. Methods

2.1 Starting material

The starting material employed in this study is a leucite-bearing phonotephrite from the 472 CE Pollena subplinian eruption of Somma-Vesuvius (Di Fiore et al., 2023; Sulpizio et al., 2005; Vona et al., 2020). Following the procedure reported by Mollo and Vona (2014) and Giuliani et al. (2024), the undoped phonotephrite (sample C10M4) was reduced to a homogeneous powder in a ball mill and grounded to pass through a #200 mesh sieve. Afterwards, the rock powder was doped with CaO produced by thermal decomposition of variable amounts of $CaCO_3$ (i.e., $CaCO_3$ *solid* + CaO *solid* + CO_2 *gas*), as CaO is an unstable compound at atmospheric pressure conditions. As detailed in Table 1, a first aliquot of the powder was doped with only ~8 (sample C18M5) or ~17 (C26M5) wt.% CaO, whereas a second aliquot of the powder was doped

158 with ~4 wt.% CaO plus addition of ~5 wt.% MgO (sample C13M8) and with ~11 wt.% CaO plus addition of
159 ~15 wt.% MgO (sample C19M17). Both undoped and doped rock powders were melted in a Fe-saturated Pt
160 crucible using a Nabertherm® furnace at 1400 °C and air redox conditions. The melt was held at constant
161 temperature for approximately 5 h and then quenched to glass in air.
162
163 *2.2 Isothermal deformation and static experiments*
164 Giuliani et al. (2024) characterized the crystal-free melt viscosity (η_{liquid}) of the doped and undoped
165 samples using high-temperature measurements with a concentric cylinder apparatus (CC) and low-temperature
166 measurements with a conventional differential scanning calorimetry (C-DSC). High-temperature
167 measurements were conducted from 1400 to 1150 °C, returning in a viscosity range from $10^{0.36}$ to $10^{2.71}$ Pa·s.
168 In contrast, low-temperature measurements were conducted from 719 to 639 °C, returning a viscosity range
169 from $10^{10.32}$ to $10^{12.28}$ Pa·s.
170 Crystallization experiments were conducted using a a Rheotronic II Rotational Viscometer equipped
171 with a concentric cylinder setup at the Experimental Volcanology and Petrology Laboratory (EVPLab) of the
172 University of Roma Tre, Rome, Italy. The system is equipped with an Anton Paar Rheolab Qc viscometer head
173 (full-scale torque of 75 mNm), a $Pt_{80}Rh_{20}$ crucible (62, 32, and 1.5 mm in height, inner diameter, and wall
174 thickness, respectively) and a $Pt_{80}Rh_{20}$ stirring spindle (3.2 and 42 mm in diameter and length, respectively).
175 The experimental setup was calibrated against the NIST 717a standard reference material, providing an
176 accuracy better than 0.06 log units (Di Fiore et al., 2021b). Temperature measurements were performed with
177 a S-type thermocouple with accuracy of ±2 °C. Two types of isothermal crystallization experiments (Table 1)
178 were conducted at ambient pressure and air oxygen fugacity: i) isothermal deformation experiments (IDEs),
179 applying shear strain rates ($\dot{\gamma}$) of 1 and 5 s^{-1}, and ii) isothermal static experiments (ISEs), conducted under
180 static conditions (i.e., no melt stirring). Prior to crystallization, a *superliquidus* pre-treatment (*Ts*) was applied
181 to ensure chemical homogenization and thermal equilibration. This involved heating the melt at 25 °C/min
182 from room temperature to 1300 or 1400 °C, then stirring the melt at a shear rate of 10 s^{-1} for 2 h. After thermal
183 pre-treatment, the melt was cooled at 25 °C/min to the *subliquidus* target temperature of 1180 °C.
184 For the ISEs, we focused on the undoped (C10M4st), CaO-doped (C18M5st and C26M5st) and
185 CaO+MgO-doped (C13M8st and C19M17st) samples. To investigate the effect of doping level on equilibrium

crystallization evolution in static conditions, experiments were performed in the absence of stirring by positioning the spindle outside the crucible. Consequently, no monitoring of the real-time viscosity evolution during crystallization is available for these experiments.

For the IDEs, two distinct experimental subsets were performed using a variable shear rate. The first subset was performed with a shear rate of 1 s^{-1}, focusing on the undoped (C10M4sr1) and all doped samples (C18M5sr1, C26M5sr1, C13M8sr1, and C19M17sr1). The second subset was performed with a shear rate of 5 s^{-1}, focusing on the undoped (C10M4sr5) and two doped samples (C18M5sr5 and C13M8sr5). The evolution of viscosity was monitored for 20-24 h, until a time-independent apparent viscosity (η_a) was achieved, indicating a stable crystal content (Chevrel et al., 2015; Di Fiore et al., 2021b; Vona and Romano, 2013).

At the end of the experimental runs, the samples were rapidly quenched using a cooling rate of ~120 °C/min by holding the crucible walls under flowing water (Campagnola et al., 2016). The quenched samples were then drilled, mounted in epoxy, and finally polished for subsequent chemical and textural analyses.

Table 1. Experimental conditions for IDEs and ISEs.

Experiment #	CaO added (wt.%)	MgO added (wt.%)	Cooling/heating rate (°C/min)	*Superliquidus* temperature (°C)	Dwell temperature (°C)	Strain rate (s^{-1})	Dwell time (h)	Pressure (MPa)	Oxygen fugacity (buffer)
ISEs									
C10M4st	0	0	25	1300	1180	0	24	0.1	air
C18M5st	7.84	0	25	1300	1180	0	24	0.1	air
C26M5st	16.81	0	25	1300	1180	0	24	0.1	air
C13M8st	3.92	5	25	1300	1180	0	24	0.1	air
C19M17st	11.21	15	25	1300	1180	0	24	0.1	air
IDEs									
C10M4sr1	0	0	25	1300	1180	1	22	0.1	air
C18M5sr1	7.84	0	25	1300	1180	1	24	0.1	air
C26M5sr1	16.81	0	25	1300	1180	1	24	0.1	air
C13M8sr1	3.92	5	25	1400	1180	1	24	0.1	air
C19M17sr1	11.21	15	25	1300	1180	1	24	0.1	air
C10M4sr5	0	0	25	1300	1180	5	24	0.1	air
C18M5sr5	7.84	0	25	1300	1180	5	22	0.1	air
C13M8sr5	3.92	5	25	1300	1180	5	24	0.1	air

2.3 Differential Scanning Calorimetry

So far the viscosity of the residual melt at a post-crystallization stage has been estimated using empirical models based on chemical composition (Giordano et al., 2008; Hui and Zhang, 2007; Langhammer et al., 2022). This approach has been extensively utilized across various studies (i.e., Campagnola et al., 2016; Chevrel et al., 2015; Di Fiore et al., 2023, 2021b; Harris et al., 2024; Kolzenburg et al., 2018; Picard et al.,

2013; Vona et al., 2011). Other studies adopted different strategies, such as the viscosity measurement of a newly synthesized melt with chemistry equivalent to that of the residual melt (e.g., Sehlke et al., 2014; Soldati et al., 2016). However, as demonstrated in our recent work (Giuliani et al., 2024), chemically-based models fail significantly to describe the crystal-free viscosity of the starting melts used in this study and, likely, the residual melts obtained after a certain degree of crystallization. Additionally, new syntheses of analogue samples may be subjected to chemical uncertainties and possibility different iron oxidation conditions (Di Fiore et al., 2024 and references therein). Therefore, to directly extract the residual melt viscosity and assess the effect of crystallization on the rheology of the magma, we have coupled conventional (C-DSC) and Flash (F-DSC) differential scanning calorimetry, as detailed below.

Conventional Differential Scanning Calorimetry (C-DSC) allows the study of the glass transition interval via the measurement of the fictive temperature (T_f) using milligrams of glass with heating rates in the range of degrees per minute. In contrast, Flash Differential Scanning Calorimetry (F-DSC) operates at much higher heating rates (thousands of degrees per second) and requires nanograms of material, making it ideal for samples that are prone to crystallization within timescales typical of C-DSC. For a detailed review, see Fanesi et al. (2025).

Building on the foundational work of Adam and Gibbs, 1965 and the model of Narayanaswamy (1971), Scherer (1984) derived a relationship between T_f and cooling rate (q in $K \cdot s^{-1}$), paralleling equilibrium viscosity (η) through a shift factor (K):

$$log_{10}\,\eta\,(T_f) = 11.3 - log_{10}(q) \quad \text{Eq. (1)}$$

This relationship was validated for basaltic melts over a range of cooling rates from 10^{-2} to 10^{6} $K \cdot s^{-1}$ (Yue et al., 2004) with a recalibrated $K = 10^{11.35}$ Pa·K. Di Genova et al. (2020b) expanded these findings using the characteristic temperature T_{onset} (i.e., T_f) to various silicate compositions, confirming a chemically invariant shift factor, $K_{onset} = 10^{11.20\pm0.15}$ Pa·K. Stevenson et al. (1995) refined the analysis by using characteristic temperatures such as T_{gpeak}, representing the peak heat flow, leading to a reformulation of Scherer's equation:

$$log_{10}\,\eta\,(T_{gpeak}) = K_{peak} - log_{10}\,(q_{c,h}) \quad \text{Eq.(2)}$$

The study of Stevenson et al. (1995) focused on SiO_2–rich melts (e.g., rhyolites) and found that K_{peak} ranges from $10^{10.1}$ to $10^{10.8}$ Pa·K as a function of the agpaitic index $\left[\left(\frac{Na_2O+K_2O}{Al_2O_3}\right)\right]$, with an average K_{peak} of $10^{10.49}$ Pa·K. Afterwards, Webb and Knoche (1996) compiled T_{peak} data for 70 silicate melt compositions in the albite–anorthite–diopside, Na_2O–SiO_2, and haplogranitic (HPG8) systems and found an average $K_{peak} = 10^{10.14}$ Pa·K from 135 data. Gottsmann et al. (2002) focused on a wide range of melts with different compositions and described K_{peak} as a composition–dependent term equal to $10^{10.321-0.175ln(x)}$ Pa·K, where x is the molar percentage of excess (network modifying) oxides. Recently, (Di Genova et al., 2023, 2020b; Fanesi et al., 2025; Giuliani et al., 2024; Scarani et al., 2022b; Stabile et al., 2021; Valdivia et al., 2024a, 2023; Zandonà et al., 2023) demonstrated that $K_{\text{onset}} = 10^{11.20\pm 0.15}$ Pa·K and $K_{\text{peak}} = 10^{9.84\pm 0.20}$ Pa·K remain chemically invariant across a wide compositional range using both iron-free and iron-bearing systems (e.g., diopside, cordierite, anorthite, spodumene, several natural silicate melts, and a peridotitic composition). These findings align with those from previous studies (e.g., Scherer, 1984; S. L. Webb and Knoche, 1996; Yue, 2008) and have been corroborated using different techniques (Di Genova et al., 2023; Valdivia et al., 2024b; Zandonà et al., 2023).

Here, to derive melt viscosity from both C-DSC and F-DSC analyses, shift-factors $K_{onset} = 11.20 \pm 0.15$ and $K_{peak} = 9.84 \pm 0.20$ were used. Giuliani et al. (2024) have recently outlined that these shift factors are constant and thus independent of melt chemistry considered in this study.

C-DSC measurements were performed with a Netzsch 404F3 Pegasus, installed at the EVPLab. The sample mass of the crystalline glass loaded into a $Pt_{80}Rh_{20}$ crucible was approximately 20 ± 5 mg. T_{onset} and T_{peak} (Fig. 1) were measured at heating and cooling rate ($q_{c,h}$) of 10 and 20 °C min^{-1}, under N_2 5.0 atmosphere (80 ml min^{-1} flow rate). The calibration of the C-DSC temperature was performed up to ~1050 °C using the melting point of different reference materials (In, Sn, Bi, Zn, Al, Ag, and Au) (Di Genova et al., 2020a; Stabile et al., 2021). Baseline measurements were conducted using two empty crucibles.

F-DSC measurements were performed with a Mettler-Toledo Flash DSC 2+, installed at the GLASS laboratory CNR-ISSMC, Rome, Italy. The instrument is equipped with a UFH1 sensor, enabling measurements up to 1,000 °C and $q_{c,h}$ of 30,000 K s^{-1}. As displayed in Fig. 1, we used $q_{c,h}$ of 1,000 and 5,000 K s^{-1}, respectively (Al-Mukadam et al., 2020; Scarani et al., 2022a). Prior to measuring the characteristic glass transition temperatures (T_{onset} and T_{peak}) of the melt, a two-step thermal treatment of an empty sensor was performed according to the manufacturer's temperature program. Initially, the temperature of the glass chip and sensor

support was set at 27 °C. Once thermal equilibrium was reached, we carried out the so-called "conditioning" program, which consists of a series of heating and cooling steps at the maximum operating temperature. Such a temperature program is required to remove the thermal history of the glass chip. Subsequently, the thermocouple correction program was carried out. F-DSC measurements were conducted on interstitial glass material from the post-run samples. Specifically, we powdered the partially crystallized quenched samples and manually isolated the interstitial glass of interest using a fine-haired pen for precise selection. To obtain an optimal signal-to-noise ratio, a glass mass ranging from ~10 to ~300 ng was used (Al-Mukadam et al., 2020). The F-DSC was calibrated using the melting temperature of aluminum (T_m = 660.4 °C) and indium (T_m = 156.6 °C).

Figure 1. Heat flow of C18M5sr1 glass measured as a function of temperature using conventional (C-DSC) and Flash (F-DSC) differential scanning calorimetry. Dashed lines correspond to the second upscan during measurements performed at 10 and 20 K min^{-1} and at 1000 and 5000 K s^{-1} using the rate-matching method (Di Genova et al., 2020b; Stabile et al., 2021; Valdivia et al., 2023).

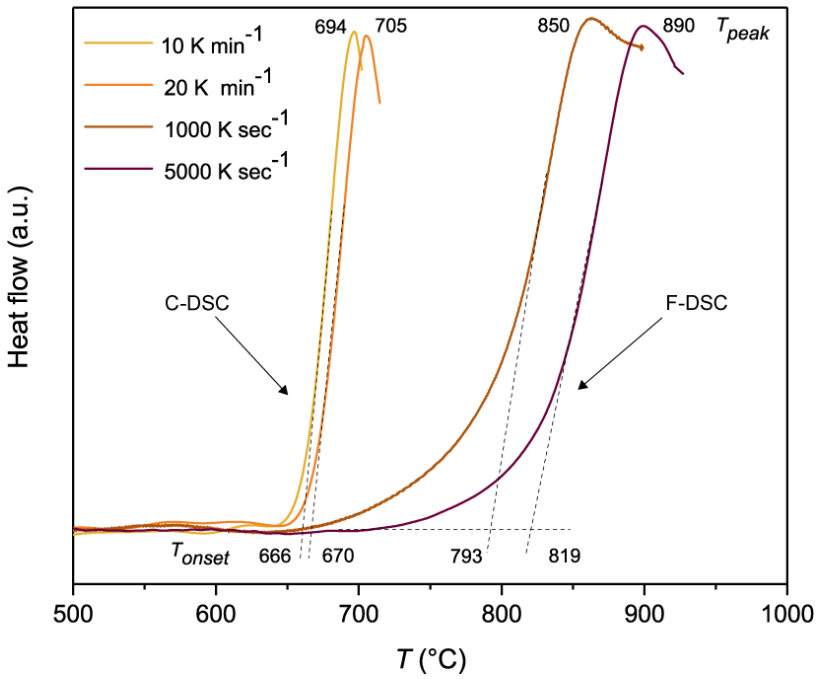

2.4 Microprobe analysis

Major element compositions of residual glasses from ISEs and IDEs (Table 2) were determined by electron probe micro-analyzer (EPMA) Cameca SX100 equipped with five WDS (wavelength dispersive) spectrometers and one EDS (energy dispersive) spectrometer and installed at the Natural History Museum in

London (UK). Analyses were performed on carbon-coated samples under high vacuum conditions, using an accelerating voltage of 15 kV and an electron beam current of 5 nA, with a defocused beam diameter of 10 μm. Elemental counting times were 15 seconds on the peak and 5 seconds on each of the two background positions. The following standards were used for calibration: jadeite (Si and Na), corundum (Al), forsterite (Mg), andradite (Fe), rutile (Ti), orthoclase (K), barite (Ba), apatite (P), and spessartine (Mn). Accuracy was better than 1–5% except for elements with abundances below 1 wt.%, for which accuracy was better than 5–10%. Precision was typically better than 1–5% for all analyzed elements.

Table 2. Microprobe analyses of the starting materials (from Giuliani et al., 2024) and residual glasses (post-ISEs and post-IDEs) resulting from isothermal static and deformation experiments. Analyses are normalized to 100%. σ represents the standard deviation of 10 microprobe analyses.

Starting material	SiO_2	TiO_2	Al_2O_3	$FeO_{tot.}$	MnO	MgO	CaO	Na_2O	K_2O	P_2O_5
C10M4	50.76	0.84	17.47	6.03	0.14	4.00	10.08	2.95	7.18	0.55
σ	0.19	0.05	0.11	0.18	0.03	0.07	0.18	0.08	0.07	0.06
C18M5	46.12	0.74	15.62	5.50	0.13	4.5	18.09	2.60	6.24	0.45
σ	0.37	0.05	0.17	0.13	0.03	0.15	0.77	0.11	0.28	0.05
C26M5	41.49	0.68	13.66	4.81	0.12	4.91	26.35	2.20	5.33	0.44
σ	0.36	0.02	0.11	0.10	0.03	0.09	0.52	0.06	0.18	0.09
C13M8	46.67	0.77	15.9	5.46	0.12	8.29	13.10	2.68	6.50	0.50
σ	0.35	0.06	0.14	0.11	0.03	0.48	0.37	0.05	0.26	0.06
C19M17	38.8	0.65	12.95	4.92	0.12	17.02	19.15	1.82	4.15	0.42
σ	1.05	0.08	0.47	0.10	0.04	1.81	0.46	0.18	0.50	0.06
post-ISEs	SiO_2	TiO_2	Al_2O_3	$FeO_{tot.}$	MnO	MgO	CaO	Na_2O	K_2O	P_2O_5
C10M4st	50.40	0.81	17.36	6.24	0.14	4.22	9.80	2.99	7.58	0.45
σ	0.45	0.02	0.14	0.02	0.01	0.04	0.06	0.07	0.09	0.02
C18M5st	47.10	0.89	16.14	6.08	0.18	4.15	15.62	3.26	6.07	0.57
σ	0.43	0.12	0.11	0.08	0.05	0.41	0.32	0.53	0.74	0.23
C26M5st	42.25	0.99	16.74	6.66	0.16	2.76	18.67	2.55	8.64	0.57
σ	0.64	0.05	0.31	0.20	0.01	0.08	0.22	0.08	0.27	0.04
C13M8st	45.53	0.83	15.74	6.21	0.15	7.26	15.00	3.22	5.63	0.43
σ	0.11	0.03	0.02	0.12	0.01	0.04	0.06	0.03	0.03	0.01
C19M17st	41.72	0.74	14.55	7.97	0.18	7.35	17.59	2.77	6.76	0.37
σ	0.72	0.01	0.19	0.02	0.01	0.16	0.21	0.02	0.14	0.03
post-IDEs	SiO_2	TiO_2	Al_2O_3	$FeO_{tot.}$	MnO	MgO	CaO	Na_2O	K_2O	P_2O_5
C10M4sr1	50.37	0.89	17.37	6.44	0.16	4.13	10.16	3.33	6.65	0.51
σ	0.36	0.02	0.20	0.01	0.01	0.03	0.02	0.05	0.11	0.03
C10M4sr5	50.62	0.87	17.05	6.69	0.16	4.39	10.05	3.24	6.38	0.56
σ	0.38	0.03	0.35	0.15	0.01	0.13	0.65	0.10	0.19	0.07

C18M5sr1	44.75	0.84	15.23	6.22	0.14	4.71	19.56	2.98	5.16	0.42
σ	0.04	0.02	0.08	0.01	0.01	0.05	0.01	0.07	0.02	0.04
C18M5sr5	46.06	0.82	15.26	6.21	0.16	4.47	17.93	3.17	5.20	0.72
σ	0.28	0.03	0.25	0.17	0.02	0.13	0.57	0.10	0.29	0.02
C26M5sr1	41.89	1.42	14.88	8.15	0.18	1.93	20.57	2.57	7.59	0.81
σ	0.36	0.05	0.32	0.45	0.01	0.26	0.46	0.10	0.01	0.04
C13M8sr1	45.99	0.81	15.52	6.28	0.15	7.19	14.87	3.36	5.39	0.45
σ	0.60	0.04	0.55	0.30	0.02	0.37	0.55	0.14	0.20	0.03
C13M8sr5	45.06	0.81	16.61	5.96	0.16	6.95	14.24	3.69	5.99	0.52
σ	0.73	0.03	0.67	0.19	0.02	0.30	0.34	0.42	0.36	0.10
C19M17sr1	41.61	0.81	15.92	6.13	0.13	7.92	17.68	3.01	6.14	0.65
σ	0.24	0.06	0.38	0.22	0.01	0.15	0.28	0.12	0.26	0.02

2.5 Textural analysis

Photomicrographs were collected at different magnifications in reflected light using both an optical microscopy and a field emission gun-scanning electron microscope FIB-SEM Scios 2 DualBeam installed at the HP-HT Laboratory of Experimental Volcanology and Geophysics of the Istituto Nazionale di Geofisica e Vulcanologia (INGV) in Rome (Italy). Backscattered electron (BSE) photomicrographs were acquired using an accelerating voltage and electron beam current of 10 kV and 0.80 nA, respectively. The ImageJ software (imagej.nih.gov/ij/) were employed for image binarization by grey level thresholding and manual drawing of crystal outlines. The error associated with the segmentation process was assessed by adding or removing pixel layers around each crystal in the binarized image. The resulting uncertainty in the crystallinity estimate is approximately ±3% (Di Fiore et al., 2023). Mean 3D crystal habits were evaluated using the *CSDslice5* software implemented by Morgan and Jerram (2006), which compares the distribution of 2D size measurements to a database of shape curves, thereby determining a best-fit 3D crystal habit in terms of short (*S*), intermediate (*I*) and long (*L*) axis. Mean crystal shapes are expressed as mean aspect ratios R_m, calculated following the method described by Vona et al. (2011). In some cases, the accurate determination of a mean crystal shape is hindered by crystal clustering and/or intergrowth.

3 Results

3.1 Phase assemblage and textural features

303 BSE photomicrographs illustrating the phase assemblage and textural features resulting from IDEs and
304 ISEs performed at 1180°C are displayed in Fig. 2. The change of mineral relations as a function of shear rate
305 and doping level is also illustrated in Fig. 3.
306 For ISEs, the undoped sample C10M4st is the only crystal-free experimental product among the entire
307 experimental set (Fig. 2). The low CaO-doped sample C18M5st is characterized by clinopyroxene-leucite
308 intergrowths (R_m = 2.2), whereas melilite dominates the mineral assemblage of the high CaO-doped sample
309 C26M5st (R_m = 3.0) (Figs. 2 and 3 and Table 3). The low CaO+MgO-doped sample C13M8st shows olivine-
310 leucite intergrowths (R_m = 2.0). This phase assemblage is replaced by spinifex olivine (R_m = 11.6) in the high
311 CaO+MgO-doped sample C19M17st (Figs. 2 and 3 and Table 3).
312 For IDEs, the mineral assemblage systematically changes as a function of both shear rate and doping
313 level (Figs. 2 and 3). In particular, the effect of convective stirring promotes the crystallization of melilite and
314 nepheline in both CaO- and CaO+MgO-doped samples. Clinopyroxene and leucite saturate the melt in
315 undoped samples C10M4sr1 and C10M4sr5, developing intricate intergrowth patterns (R_m = 3.5 and R_m = 1.9,
316 respectively). The low CaO-doped samples C18M5sr1 and C18M5sr5 are characterized by the crystallization
317 of clinopyroxene, leucite and melilite (R_m = 3.5 and R_m = 2.1, respectively). Clinopyroxene disappears in the
318 high CaO-doped sample C26M5sr1, whereas melilite and nepheline expand their stability fields (R_m = 4.5)
319 (Figs. 2 and 3 and Table 3). The low CaO+MgO-doped samples C13M8sr1 and C13M8sr5 (R_m = 2.9 and R_m
320 = 1.9, respectively) exhibit olivine, clinopyroxene and leucite, either as individual crystals or intergrowth
321 relations. Clinopyroxene is no longer stable in the high CaO+MgO-doped sample C19M17sr1 (R_m = 2.6),
322 whereby olivine, nepheline and melilite crystallize (Figs. 2 and 3).
323
324
325
326
327
328

Figure 2. BSE photomicrographs illustrating the phase assemblage and textural features resulting from ISEs and IDEs. Gl, glass. Ol, olivine. Cpx, clinopyroxene. Lct, leucite. Nph, nepheline. Mll, melilite

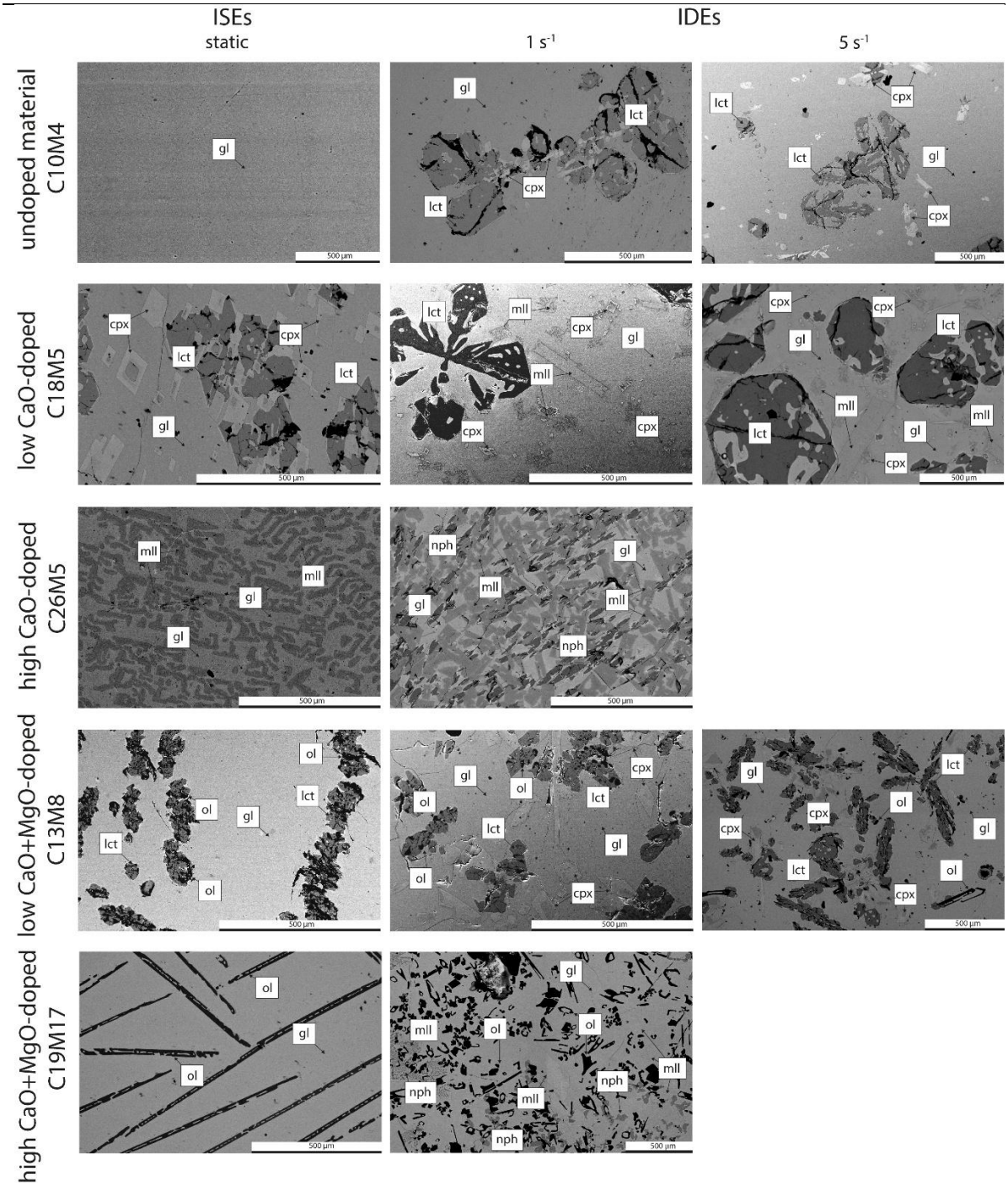

Figure 3. Mineral relations as a function of shear rate and doping level in ISEs and IDEs. Plots (a) and (b) illustrate the mineral phases of CaO-doped and CaO+MgO-doped samples, respectively. Ol, olivine. Cpx, clinopyroxene. Lct, leucite. Nph, nepheline. Mll, melilite. The dashed lines qualitatively indicate the in-out saturation conditions of crystalline phases and serve as a visual guide. The exact boundaries between data points remain uncertain.

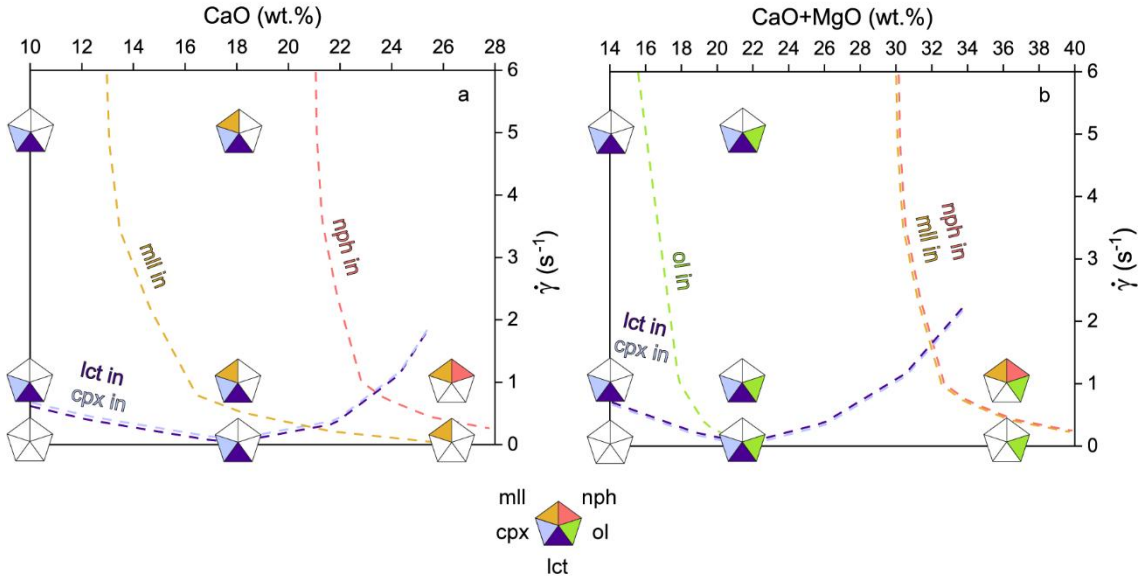

3.2 Crystal fraction

Fig. 4 shows the crystal fraction (Φ) of ISEs and IDEs as a function of shear rate and doping level (see also Table 3 for further quantitative details).

For ISEs, the magnitude of Φ increases from ~32% to ~43% with increasing the doping level of CaO in samples C18M5st and C26M5st compared to the crystal-free undoped sample C10M4st (Fig. 4). Conversely, the value of Φ is significantly lower in samples C13M8st (Φ ~10%) and C19M17st (Φ ~8%) doped with CaO+MgO (Fig. 4).

For IDEs, as the doping level of CaO and CaO+MgO increases, the magnitude of Φ increases at constant shear rate with exception of sample C19M17sr1 (Fig. Table 3 and Fig. 4). Increasing convective stirring generally increases the crystal fraction, except for sample C18M5sr1. For the undoped samples C10M4sr1 and C10M4sr5, Φ increases from ~16% to ~19% as the shear rate increases from 1 to 5 s^{-1}, respectively (Fig. 4). For the weakly CaO-doped samples C18M5sr1 and C18M5sr5, Φ increases from ~24% to ~31%. Notably, for the highly CaO-doped sample C26M5sr1, Φ significantly increases up to ~51% (Fig. 4). On the other hand, for the low CaO+MgO-doped samples C13M8sr1 and C13M8sr5, Φ increases from

~30% to ~35% with increasing the shear rate. For the highly CaO+MgO-doped sample C19M17sr1, Φ is ~31% (Fig. 4). These findings collectively suggest that, at high doping levels, the addition of CaO+MgO is less effective in enhancing the crystallization process compared to the addition of only CaO.

Table 3. Phase abundance in ISEs and IDEs. The numbers in parentheses represent the aspect ratios (R) of each mineral phase, while for total crystallinity, they indicate the mean aspect ratio (R_m) calculated as reported in Vona et al. (2011).

Experiment	Olivine	Clinopyroxene	Leucite	Nepheline	Melilite	Glass	Total crystallinity
	Φ_{ol} (%)	Φ_{cpx} (%)	Φ_{lct} (%)	Φ_{nph} (%)	Φ_{mll} (%)	Φ_{glass} (%)	Φ_{tot} (%)
ISEs							
C10M4st	-	-	-	-	-	100	-
C18M5st	-	10 (2.3)	22 (2.2)	-	-	68	32 (2.2)
C26M5st	-	-	-	-	43 (3.0*)	100	43 (3.0*)
C13M8st	5 (2.0*)	-	5 (2.0*)	-	-	90	10 (2.0*)
C19M17st	8 (11.6)	-	-	-	-	92	8 (11.6)
IDEs							
C10M4sr1	-	7 (3.0)	9 (4.0)	-	-	84	16 (3.5)
C18M5sr1	-	2 (2.2)	19 (2.6)	-	3 (10)	79	24 (3.5)
C26M5sr1	-	-	-	6 (4.5*)	45 (4.5*)	94	51 (4.5*)
C13M8sr1	2 (5.0)	11 (3.0)	17 (2.7)	-	-	70	30 (2.9)
C19M17sr1	17 (2.0)	-	-	2 (4.5)	10 (3.4)	81	29 (2.6)
C10M4sr5	-	3 (1.7)	16 (2.0)	-	-	81	19 (1.9)
C18M5sr5	-	5 (4.0)	17 (2.0)	-	9 (1.6)	78	31 (2.1)
C13M8sr5	3 (5.0)	17 (1.6)	15 (2.0)	-	-	65	35 (1.9)

* crystal clustering and/or intergrowth prevents the accurate determination of a mean crystal habit elongation.

Figure 4. 3D histogram plot showing the crystal fraction evolution of ISEs and IDEs as a function of both shear rate (0, 1, and 5 s^{-1}) and CaO (left diagram; CaO = 10, 18, 26 wt.%) and CaO+MgO (right diagram; CaO+MgO = 15, 21, 36 wt.%) doping levels. The dotted square refers to the crystal-free static sample C10M4st. Ol, olivine. Cpx, clinopyroxene. Lc, leucite. Nph, nepheline. Mll, melilite.

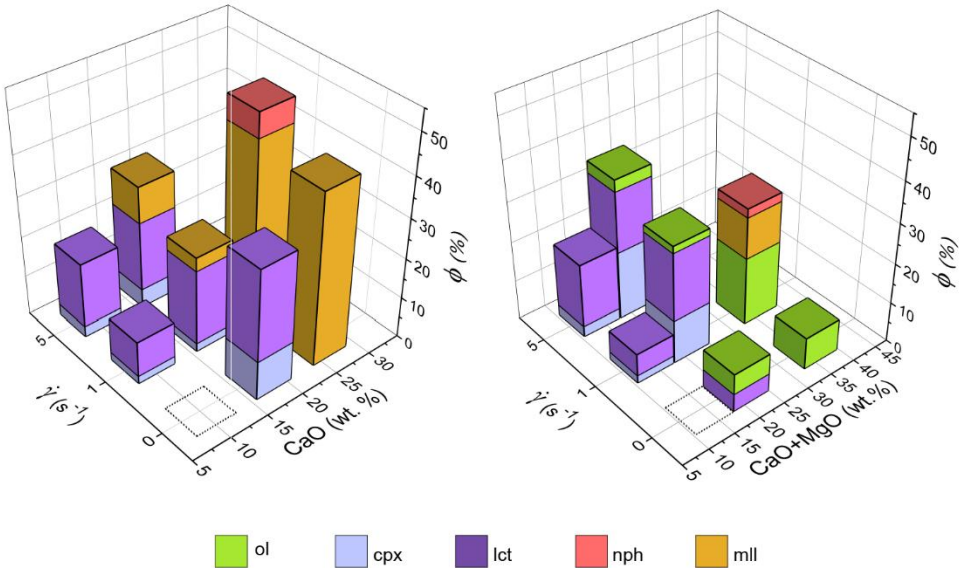

3.3 Chemical evolution of starting and residual glasses

According to the TAS classification diagram (total alkali vs. silica; Le Bas et al., 1986), the composition of the starting glass shifts from a more differentiated phonotephrite (~51 wt.% SiO_2 and ~10 wt.% Na_2O+K_2O) for the undoped sample C10M4 to a less differentiated phonotephrite for samples C18M5 (~46 wt.% SiO_2 and ~9 wt.% Na_2O+K_2O) and C13M8 (~47 wt.% SiO_2 and ~9 wt.% Na_2O+K_2O) weakly doped with CaO and CaO+MgO, respectively (Fig. 5). Conversely, the composition of the starting glass corresponds to that of a foidite for samples C26M5 (~41 wt.% SiO_2 and ~8 wt.% Na_2O+K_2O) and C19M17 (~39 wt.% SiO_2 and ~6 wt.% Na_2O+K_2O) highly doped with CaO and CaO+MgO, respectively (Fig. 4). As a general rule, the addition of increasing amounts of CaO and CaO+MgO produces starting glasses that are progressively depleted in SiO_2 and Na_2O+K_2O, thus reproducing both juvenile materials and skarn xenoliths erupted at Somma-Vesuvius (Fig. 5). At the same time, the amounts of CaO and MgO in these compositions increase from ~10 to ~26 wt.% and from ~4 to ~17 wt.%, respectively, in response to carbonate assimilation (Table 2).

The compositions of residual glasses from static (i.e., C10M4st) and stirring experiments (i.e., C10M4sr1 and C10M4sr5) carried out on the undoped sample C10M4 cluster at the boundary between phonotephrite and tephriphonolite (~50-51 wt.% SiO_2 and ~10-11 wt.% Na_2O+K_2O; Fig. 5). Similarly, residual glasses obtained using as starting compositions samples C18M5 (i.e., C18M5st, C18M5sr1 and C18M5sr1) and C13M8 (i.e., C13M8 and C13M8r1) weakly doped with CaO and CaO+MgO, respectively, cluster at the boundary between tephrite and phonotephrite (~45-47 wt.% SiO_2 and ~8-9 wt.% Na_2O+K_2O; Fig. 5). The only

exception is found for the residual glass C13M8sr5, which is placed at the boundary between phonotephrite and foidite (~45 wt.% SiO_2 and ~10 wt.% Na_2O+K_2O; Fig. 5). On the other hand, residual glasses from static and stirring experiments carried out on samples C26M5 (i.e., C26M5st and C26M5sr1) and C19M17 (i.e., C19M17st and C19M17sr1) highly doped with CaO and CaO+MgO, respectively, exhibit a more marked differentiation trend within the foidite field (up to ~42 wt.% SiO_2 and ~11 wt.% Na_2O+K_2O; Fig. 5).

It is worth noting that residual glasses resulting from undoped samples and weakly doped CaO and CaO+MgO samples correspond to the compositions of juvenile materials erupted at Somma-Vesuvius, whereas residual glasses from highly doped CaO and CaO+MgO samples fall within the field of skarn xenoliths (Fig. 5 and S1).

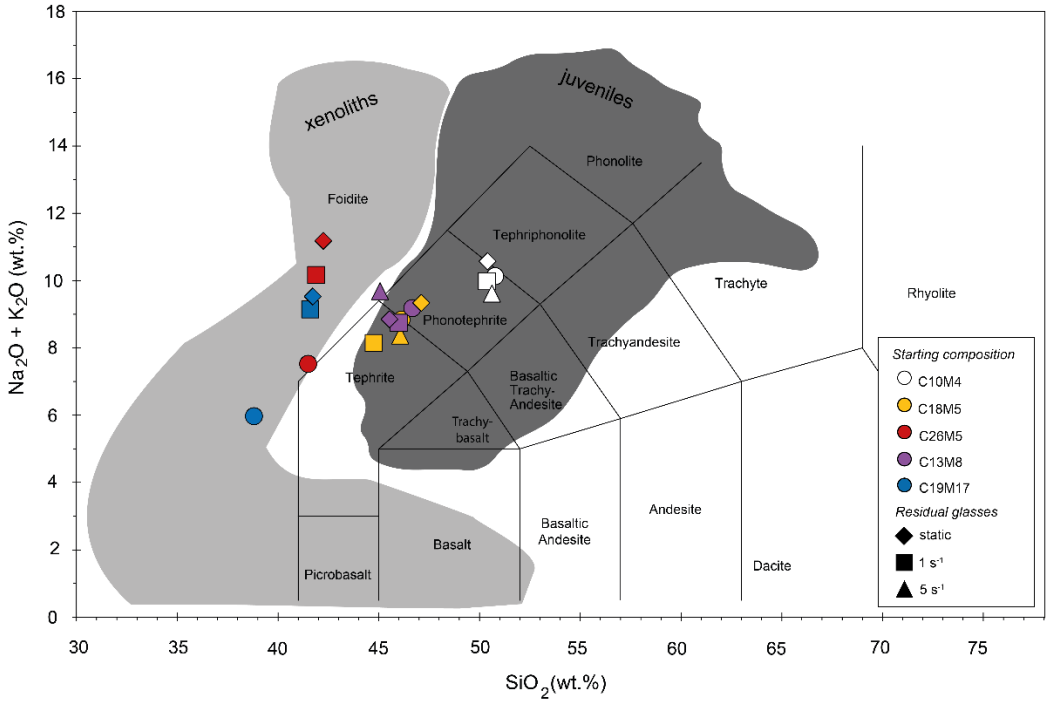

Figure 5. Total alkali vs. silica (TAS) diagram showing the compositions of undoped and doped starting glasses and residual glass. The undoped starting material (C10M4) is represented as a white circle. CaO-doped starting glasses are represented by the yellow (C18M5) and red (C26M5) circles, whilst purple (C13M8) and blue (C19M17) circles correspond to CaO+MgO-doped starting glasses. Diamonds refer to residual glasses from ISEs. Squares and triangles refer to residual glasses from IDEs. The dark grey and light grey fields represent juvenile materials (Jolis et al., 2015; Macdonald et al., 2016; Rosi and Santacroce, 1983; Santacroce et al., 2008) and skarn xenoliths (Del Moro et al., 2001; Fulignati et al., 2004, 2000; Jolis et al., 2015) erupted at Somma-Vesuvius.

3.4 Apparent viscosity evolution and post-run sample deformation

In IDEs, the temporal evolution of the apparent viscosity (η_a) and shear stress (τ) measured at 1180 °C for undoped and doped samples is illustrated in Fig. 6 (shear rate of 1 s^{-1}) and Fig. 7 (shear rate of 5 s^{-1}). These different experiments display complex patterns of increasing viscosity and rheological response. A detailed list and schematic graph of rheological parameters, such as the peak apparent viscosity ($\eta_{a\ peak}$), minimum apparent viscosity ($\eta_{a\ min}$), peak stress (τ_{peak}), peak time (t_{peak}) and the timespan (t_a) to achieve the stable apparent viscosity (η_a), is reported in Table 4 and in Fig. S2.

The undoped samples C10M4sr1 (Fig. 6a) and C10M4sr5 (Fig. 7a) show that the apparent viscosity increases with time in response to the thermal relaxation of the melt, as its structural framework adjusts from the *superliquidus* state (1300-1400 °C) to the target temperature of 1180 °C. After ~30 min at 1180 °C, η_a first stabilizes to $10^{2.62}$ Pa·s (C10M4sr1) and $10^{2.75}$ Pa·s (C10M4sr5), before increasing to $10^{2.77}$ Pa·s and $10^{2.84}$ Pa·s, respectively. Since these experiments were conducted at constant shear rate, with $\tau = \mu\dot{\gamma}$, the corresponding value of τ mirrors the evolutionary trend of viscosity, attaining $10^{2.77}$ (C10M4sr1) and $10^{3.50}$ Pa (C10M4sr5). The surface morphology of the recovered samples is smooth, indicating that both the samples deformed viscously upon the applied shear rate (Fig. 8a).

Low CaO-doped samples C18M5sr1 (Fig. 6b) and C18M5sr5 (Fig. 7b) exhibit a more complex apparent viscosity evolution, which is characterized by an initial steep increase up to a maximum peak value and a subsequent viscosity (and stress) drop. Afterwards, the increase in apparent viscosity is more smoothed. For sample C18M5sr1, a gentle viscosity increase shows a sawtooth profile made up of subtle viscosity drops and recoveries (Fig. 6b). The apparent viscosity starts to increase after ~10 h and a peak value of log $10^{2.94}$ Pa·s (at $10^{2.94}$ Pa) is achieved ~5 h later. After a local minimum of $10^{2.57}$ Pa·s, a stable viscosity of $10^{2.96}$ Pa·s is attained at the end of the measurement (23 h). For sample C18M5sr5, the apparent viscosity starts to increase after ~4 h and a peak value of $10^{2.75}$ Pa·s (as $10^{3.40}$ Pa) is achieved ~12 h later. After a local minimum of $10^{2.56}$ Pa·s, a stable viscosity of $10^{2.63}$ Pa·s is attained at the end of the measurement (20 h). The high CaO-doped sample C26M5sr1(Fig. 6c) exhibits a rapid increase in apparent viscosity up to $10^{4.33}$ Pa·s (at $10^{4.33}$ Pa) after ~1 h and 20 min, then followed by a gradual decline to a stable value of $10^{3.34}$ Pa·s (22 h).

Low CaO+MgO-doped samples C13M8sr1 (Fig. 6d) and C13M8sr5 (Fig. 7d) show apparent viscosity trends like those observed for the low CaO-doped samples, with a viscosity peak followed by a drop. For

419 sample C13M8sr1, there is an initial rise in apparent viscosity after ~3 h, peaking at $10^{3.85}$ Pa·s (and $10^{3.85}$ Pa)
420 ~2 h later, and declining to a stable viscosity of $10^{3.00}$ Pa·s ~17 h later. For sample C13M8sr5, there is a marked
421 initial increase in apparent viscosity after ~2 h, peaking at about $10^{3.23}$ Pa·s (and $10^{3.90}$ Pa) and followed by a
422 further increase in apparent viscosity before stabilization at $10^{2.98}$ Pa·s (20 h). For the high CaO+MgO doped
423 sample C19M17sr1 (Fig. 6e), a rapid increase in apparent viscosity is observed, peaking at $10^{3.12}$ Pa·s (and
424 $10^{3.12}$ Pa) within ~2 h. Afterwards, the apparent viscosity gradually decreases to $10^{2.98}$ Pa·s, then increases
425 again and becomes stable at $10^{3.12}$ Pa·s until the end of the experiment (22 h).

426 Notably, the examination of the surface morphology of all CaO and CaO+MgO-doped samples reveals
427 that the applied deformation regime induces a non-homogenous deformation characterized by viscous rupture
428 and fracture development (Fig. 8b).

429

Figure 6. Temporal evolution of the apparent viscosity (η_a) for samples (a) C10M4sr1, (b) C18M5sr1, (c) C26M5sr1, (d) C13M8sr1 and (e) C19M17sr1 at 1180 °C upon the effect of a shear rate ($\dot{\gamma}$) of 1 s^{-1}. The apparent viscosity is expressed as 'crystallization exp' (solid line). The crystal-free viscosity of the starting glass (dotted line) from Giuliani et al. (2024), the crystal-free viscosity of the residual glass (dashed line; see section 3.5) and the melt+crystal viscosity (solid line) calculated using the model of Frontoni et al. (2022) (see section 4.2.3) are also presented for comparison in the figure. The modeling results for sample C26M5sr1 ($\log\eta_{am}$ = 7.85 Pa·s) are out of scale and therefore not displayed in the figure.

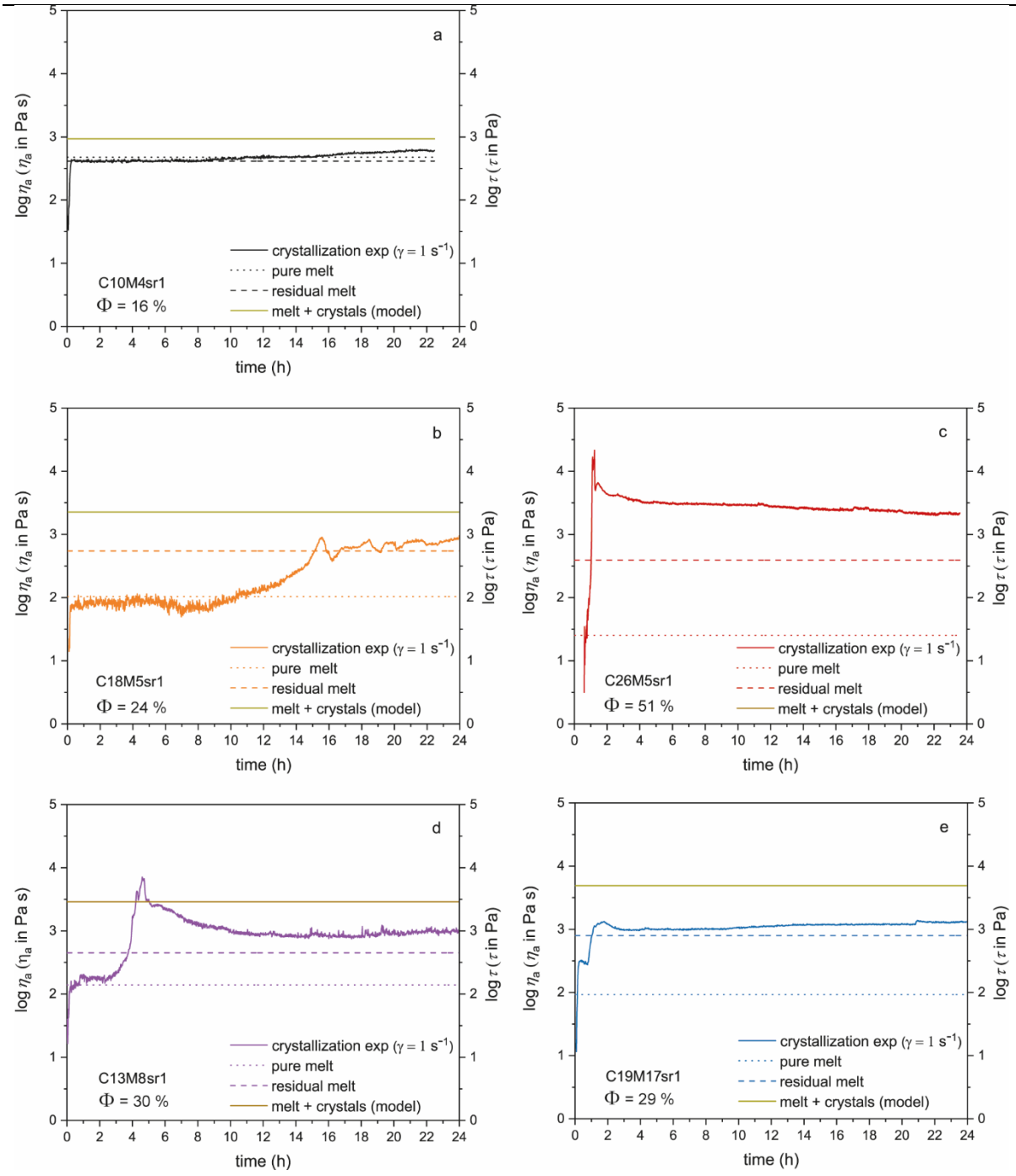

Figure 7. Temporal evolution of the apparent viscosity (η_a) for samples (a) C10M4sr5, (b) C18M5sr5, (c) C13M8sr5 at 1180 °C upon the effect of a shear rate ($\dot{\gamma}$) of 5 s^{-1}. The apparent viscosity is expressed as 'crystallization exp' (solid line). The crystal-free viscosity of the starting glass (dotted line) from Giuliani et al. (2024), the crystal-free viscosity of the residual glass (dashed line; see section 3.5), and the melt+crystal viscosity (solid line) calculated using the model of Frontoni et al. (2022) (see section 4.2.3) are also presented for comparison in the figure.

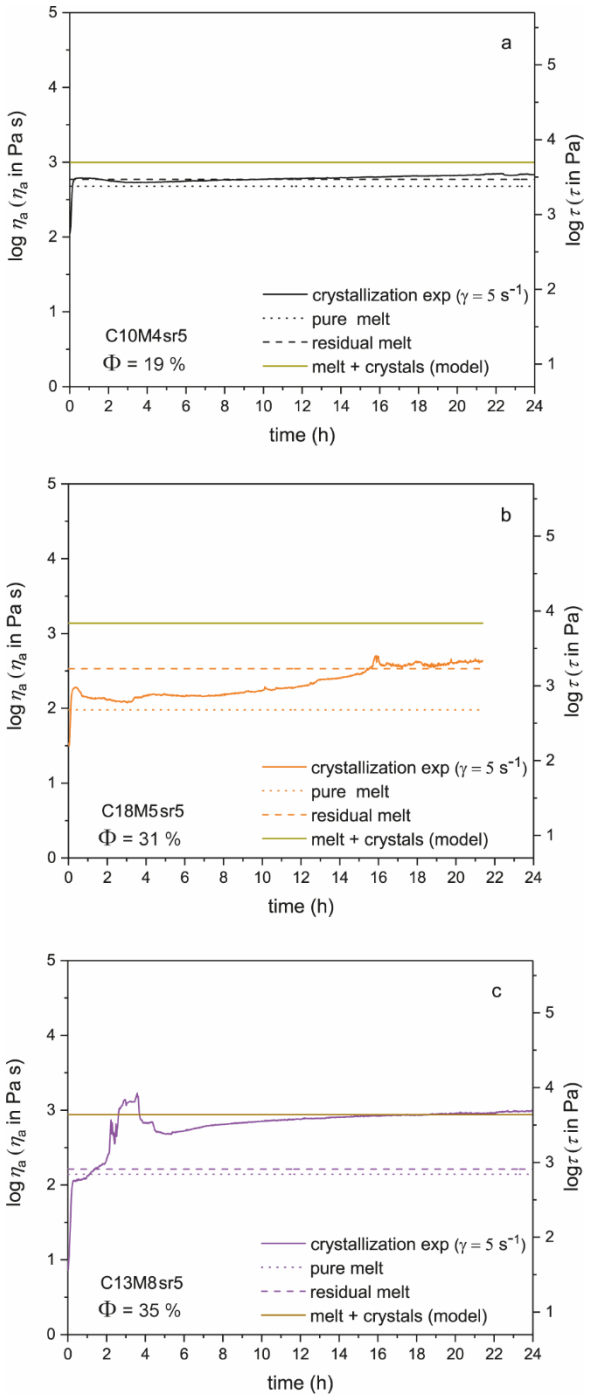

433

434

435

436

437

438

439

Table 4. Results of viscosity measurements from IDEs.

	peak apparent viscosity	peak stress	peak time	minimum apparent viscosity	timeline of stable viscosity	stable apparent viscosity
	$\eta_{a\,peak}$	τ_{peak}	t_{peak}	$\eta_{a\,min}$	t_a	η_a
	$\log_{10}\eta$ (η in Pa·s)	$\log_{10}\tau$ (τ in Pa)	h (hours)	$\log_{10}\eta$ (η in Pa·s)	h (hours)	$\log_{10}\eta$ (η in Pa·s)
C10M4sr1	-	-	-	-	20	2.77
C18M5sr1	2.94	2.94	15	2.57	23	2.96
C26M5sr1	4.33	4.33	1	-	22	3.34
C13M8sr1	3.85	3.85	5	-	22	3.00
C19M17sr1	3.12	3.12	3	2.98	22	3.12
C10M4sr5	-	-	-	-	20	2.84
C18M5sr5	2.75	3.40	16	2.56	20	2.63
C13M8sr5	3.23	3.90	4	2.68	22	2.98

440

441

Figure 8. Surface morphologies of representative post-experimental samples. (a-b) Post-experimental surface morphology of the samples recovered at the end of IDEs, showing two different rheological behaviors: (a) viscous deformation (sample C10M4sr1) and (b) viscous/brittle rupture (Sample C26M5sr1). Note that the hole at the center of the crucible indicates the spindle position. In (b), the high crystal content (brown color) and the presence of crystal aggregates lead to the development of large fractures. The inner diameter of the crucible is 32 mm.

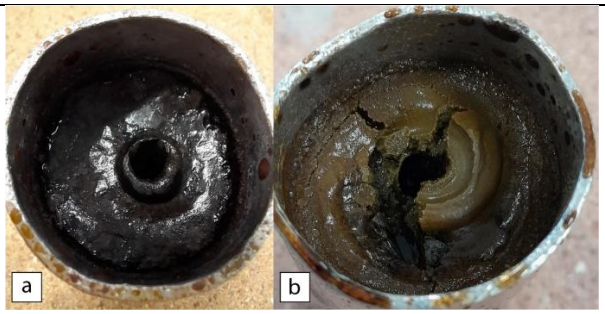

442

443

444

445

446

447 *3.5 Viscosity of residual glasses*

448 For all residual glasses, both T_{onset} and T_{peak} from C-DSC and F-DSC measurements increase with
449 increasing cooling/heating rate ($q_{c,h}$). The residual glass C10M4sr5 exhibits the lowest T_{onset} and T_{peak} for a
450 given $q_{c,h}$, whilst the residual glass C13M8sr5 displays the highest values of T_{onset} and T_{peak}. The remaining
451 residual glasses fall in between these two end-members (Table 5). This suggests that variations in chemical
452 composition influence the structural relaxation of the melt.

453 The residual melt viscosity (η_o), calculated by Eq. (3) at T_{onset} and T_{peak} from C-DSC and F-DSC
454 measurements (Table 5), ranges from $10^{6.14}$ to $10^{11.98}$ Pa·s for temperatures varying from 890 and 638 °C (Figs.
455 1 and 9).

456

Table 5. Low temperature viscosity data derived by C-DSC and F-DSC.

sample		$T_{10onset}$	$T_{20onset}$	$T_{1000onset}$	$T_{5000onset}$	T_{10peak}	T_{20peak}	$T_{1000peak}$	$T_{5000peak}$
C10M4sr1	°C	650	658	773		685	694	834	
	logη (η in Pa·s)	11.98	11.68	8.19		10.62	10.32	6.34	
C18M5sr1	°C	666	670	793	819	694	705	850	890
	logη (η in Pa·s))	11.98	11.68	8.19	7.49	10.62	10.32	6.34	6.14
C26M5sr1	°C	647	654	772		684	694	826	
	logη (η in Pa·s)	11.98	11.68	8.19		10.62	10.32	6.34	
C13M8sr1	°C	652	661	777		681	697	839	
	logη (η in Pa·s)	11.98	11.68	8.19		10.62	10.32	6.34	
C19M17sr1	°C	658	662	787		693	700	856	
	logη (η in Pa·s)	11.98	11.68	8.19		10.62	10.32	6.34	
C10M4sr5	°C	638	645	780		675	688	836	
	logη (η in Pa·s))	11.98	11.68	8.19		10.62	10.32	6.34	
C18M5sr5	°C	665	672	785	815	698	704	838	877
	logη (η in Pa·s))	11.98	11.68	8.19	7.49	10.62	10.32	6.34	6.14
C13M8sr5	°C	650	658	764		661	695	815	
	logη (η in Pa·s)	11.98	11.68	8.19		10.62	10.32	6.34	

457

458

459 To model the temperature dependence of viscosity, data were fitted using the MYEGA equation
460 (Mauro et al., 2009), which requires values for the viscosity at infinite temperature ($log\ \eta_\infty$), the glass
461 transition temperature (T_g) and the melt fragility (m):

462

463 $$\log_{10}\eta_s(T) = \log_{10}\eta_\infty + (12 - \log_{10}\eta_\infty)\frac{T_g}{T}\exp\left[\left(\frac{m}{12-\log_{10}\eta_\infty} - 1\right)\left(\frac{T_g}{T} - 1\right)\right] \qquad \text{Eq. (3)}$$

The viscosity at infinite temperature is set to -2.93 (Langhammer et al., 2022; Zheng et al., 2011), T_g corresponds to the temperature at which the viscosity is 10^{12} Pa·s (i.e. $T_{10onset}$; Scherer, 1984; Table 5), and m is a fit parameter. Residual melt viscosity data derived from C-DSC are similar to those obtained for the starting melts (Giuliani et al., 2024; Fig. 7), although samples C10M4sr5 and C26M5sr1 exhibit larger deviations. When considering data from F-DSC, the MYEGA fits for the residual melts markedly deviate from those of the starting melts, showing crossovers at high temperatures for the undoped samples (i.e., C10M4sr1 and C10M4sr5) and at low temperatures for the CaO (i.e., C18M5sr1, C18M5sr5, and C26M5sr1) and CaO+MgO (C13M8sr1, C13M8sr5, and C19M17sr1) doped samples. The melt fragility, which illustrates how the melt viscosity changes with temperature around T_g, returns a broad range of values across the samples. The highest melt fragility is observed for sample C13M8sr5 (40.04), indicating that the viscosity increases more rapidly with cooling than other samples. The lower melt fragility of sample C19M17sr1 (35.44) suggests an opposite behavior, highlighting differences in thermal dynamics due to varying chemical compositions (Table 6).

Table 6 shows the residual melt viscosities at 1180 °C, the temperature at which the crystallization experiments were performed. The modeled viscosity indicates a viscosity generally higher than that measured for the starting glasses, but lower than the melt+crystal viscosity measured from IDEs (Fig. 10). In the undoped samples C10M4sr1 and C10M4sr5, the viscosities are relatively consistent to $10^{2.62}$ and $10^{2.77}$ Pa·s, respectively. In contrast, CaO-doped samples exhibit significant variations in viscosity across different doping levels and shear rates. At low CaO-doping levels, the sample C18M5sr1 (shear rate of 1 s^{-1}) displays a higher residual viscosity compared to sample C18M5sr5 (shear rate of 5 s^{-1}), as well as compared to the high CaO-doped sample C26M5sr1. Conversely, at low CaO+MgO-doping levels, the sample C13M8sr1 (shear rate of 1 s^{-1}) shows a residual viscosity higher than that derived for the sample C13M8sr5 (shear rate of 5 s^{-1}). The highest residual viscosity is calculated for the high CaO+MgO-doped sample C19M17sr1.

Table 6. Glass transition temperature (T_g) measured by C-DSC. Melt fragility (m) and viscosity of the residual glasses (η_o) from IDEs are calculated at 1180 °C through the MYEGA equation from Mauro et al. (2009). The relative viscosity (η_r) is calculated as the ratio of the apparent viscosity of the suspension (η_a) to the viscosity of the residual melt (η_o). The net effect of the crystallinity on the viscosity η_{rm} and modeled apparent viscosity η_{am} are calculated using the model of Frontoni et al. (2022). The difference between measured and modeled relative viscosities is expressed as $\Delta\eta_r$.

	T_g	m	$\log\eta_o$	$\log\eta_r$	$\log\eta_{rm}$	$\log\eta_{am}$	$\log\Delta\eta_r$
	(°C)		(η in Pa·s)			(η in Pa·s)	
C10M4sr1	649	36.89	2.62	0.15	0.33	2.95	0.18
C18M5sr1	666	37.43	2.74	0.22	0.61	3.34	0.39
C26M5sr1	647	36.81	2.59	0.75	5.25	7.85	4.50
C13M8sr1	652	36.83	2.65	0.33	0.82	3.47	0.49
C19M17sr1	658	35.44	2.90	0.21	0.74	3.64	0.53
C10M4sr5	638	32.02	2.77	0.07	0.31	3.08	0.24
C18M5sr5	665	38.91	2.53	0.10	0.63	3.16	0.53
C13M8sr5	650	40.04	2.21	0.77	0.73	2.94	-0.04

490

491

492

493

Figure 9. Temperature-dependence of the viscosity measured for starting (Giuliani et al., 2024) and residual glasses (this study). The MYEGA fits from the equation of Mauro et al. (2009) refer to viscosity data obtained by C-DSC and F-DSC measurements at low and high temperature regimes. The viscosities of starting melts are displayed as solid lines and circles (Giuliani et al., 2024). The viscosities of residual melts and their modelling are displayed as squares and dashed lines for a shear rate of 1 s^{-1}, and triangles and dotted lines for a shear rate of 5 s^{-1}. The melt+crystal viscosities from IDEs performed at 1180 °C are also displayed as diamonds and inverted triangles for shear rates of 1 and 5 s^{-1}, respectively. The panels show the temperature-dependence of the viscosity measured for the undoped sample C10M4 (a), the low CaO-doped sample C18M5 (b), the high CaO-doped sample C26M5 (c), the low CaO+MgO-doped sample C13M8 (d), and the high CaO+MgO-doped sample C19M17 (e).

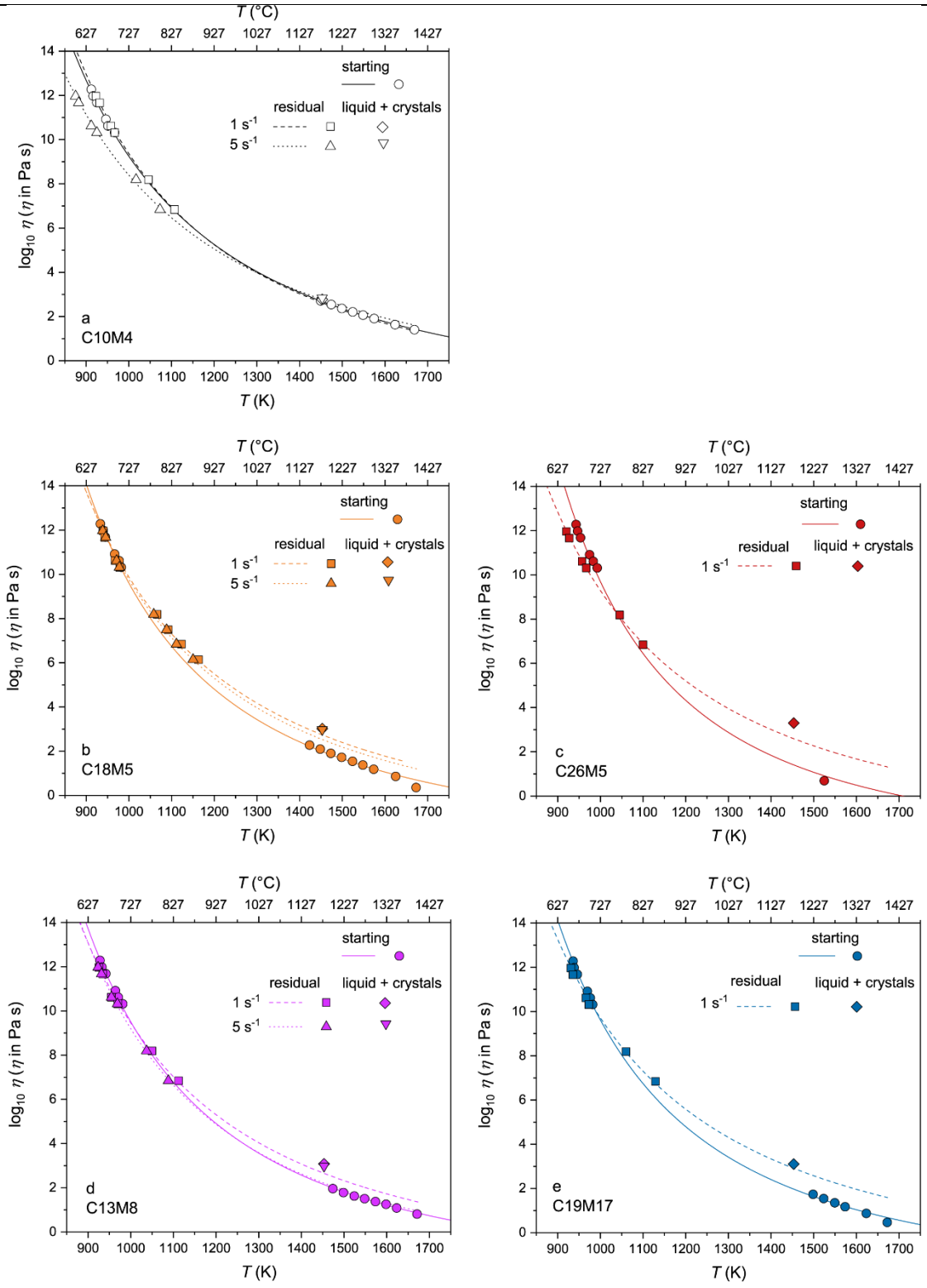
T (°C)
627 727 827 927 1027 1127 1227 1327 1427
starting
residual
liquid + crystals
1 s-1
5 s-1
log10 η (η in Pa s)
a
C10M4
T (K)
900 1000 1100 1200 1300 1400 1500 1600 1700
b
C18M5
c
C26M5
d
C13M8
e
C19M17

4 Discussion

4.1 Effect of carbonate assimilation and shear rate on the crystallization rate and mineral assemblage

Results from both IDEs and ISEs provide essential insights into how shear rate and carbonate assimilation reactions affect the crystallization rate and mineral assemblage of silica undersaturated melts (Figs. 2 and 3). At 1180 °C, the crystal fraction significantly increases as a function of doping level (Fig. 4 and Table 3), pointing out that carbonate assimilation promotes melt crystallization (e.g., Mollo et al., 2010; Mollo and Vona, 2014). As pointed out by Giuliani et al. (2024), ionic potential of Mg^{2+} and competition with Ca^{2+} cations for bonding with oxygen limit the ability of MgO addition to break down the silicate network thus causing a weaker effect on melt viscosity. The reduced impact of doping on melt viscosity in the CaO+MgO-doped system (C13M8 and C19M17 starting materials) results in higher overall viscosity compared to samples doped exclusively with CaO (C18M5 and C26M5 starting materials). This increased viscosity restricts the mobility of the constituent elements, thereby limiting their ability to rearrange and crystallize. A similar trend is also observed under convective stirring conditions, emphasizing the pivotal role of melt compositional changes in driving the dynamic crystallization of decarbonated magmas. Shear rate is observed to enhance crystallization by promoting atomic collisions and by transporting fresh melt to the surfaces of pre-existing crystals, and these processes also lead to the development of more euhedral and equant crystal habits (Table 3; cf. Mollo et al., 2024)

Under these deformation conditions, the residual glasses exhibit minimal compositional variations, except in highly doped samples, where a shift towards alkali-rich compositions is observed (Figs. 5 and Table 2). Viscosity measurements reveal a direct correlation between these chemical and physical changes with rheological properties, outlining that both doping and shear rate contribute to increased viscosity and more complex rheological behavior (Figs. 6 and 7, and Table 4).

The experimental phase assemblage closely resembles the paragenesis of skarn rocks from different igneous systems worldwide (e.g., Del Moro et al., 2001; Fulignati et al., 2004; Gaeta et al., 2000; Lustrino et al., 2022; Wenzel et al., 2002; Whitley et al., 2020). The ubiquitous crystallization of clinopyroxene in both undoped and doped samples (Fig. 3) is caused by the enlargement of its stability field upon the effect of carbonate assimilation (cf. Iacono Marziano et al., 2008; Mollo et al., 2010). Olivine is observed exclusively in samples doped with CaO+MgO (Fig. 3), consistent with previous magma-carbonate interaction experiments

documenting that dolomite assimilation, as an MgO-bearing mineral phase, promotes olivine crystallization (Iacono Marziano et al., 2007). Leucite remains stable in the undoped phonotephritic sample and at low doping levels but disappears in highly CaO- and CaO+MgO-doped samples (Fig. 3). This observation aligns with natural juvenile products from Somma-Vesuvius, where leucite is a low-pressure ($P \leq 100$ MPa) mineral phase in equilibrium with phonotephritic melts (Fulignati et al., 2004). The crystallizing margins of the shallow magma chamber feeding eruptions at Somma-Vesuvius are represented by glass-bearing fergusites, consisting of highly crystalline rocks composed primarily of leucite, clinopyroxene, and olivine, among other minerals (Del Moro et al., 2001). Magmas are progressively contaminated by the addition of CaO and MgO derived from the host rocks, thus leading to abundant clinopyroxene crystallization and accumulation in the lower portion of the chamber. Clinopyroxenitic nodules found in volcanic deposits testify to crystal accumulation by crystal settling (Del Moro et al., 2001). On the other hand, skarn rocks at Somma-Vesuvius are mainly represented by melilite-bearing xenoliths with minor nepheline, particularly skarn xenoliths found in 1944 and AD 472 eruption deposits (Fulignati et al., 2004). Our experiments support the hypothesis proposed by Fulignati et al. (2004) that melilite crystallization is primarily driven by the assimilation of calcite rather than dolomite (Fig. 3), occurring through the high-temperature ($T \geq 950$ °C) magma contamination reaction: $CaMgSi_2O_6$ (*diopside*) + $CaCO_3$ (*calcite*) = $Ca_2MgSi_2O_7$ (*akermanite, melilite group*). It is important to emphasize that this reaction shifts to the left with increasing stirring (Fig. 3), as enhanced convective mixing promotes greater ion mobility, thereby favoring crystallization. An increased crystal fraction leads to strong silica undersaturation and the formation of feldspathoids which resemble feldspars but have a different structure and much lower silica content.

While clinopyroxene and leucite are generally euhedral in both undoped and doped samples, as observed in natural skarn rocks, a key finding of our experiments is the growth of anhedral olivine and melilite crystals (Fig. 2). The morphology of these mineral phases is strongly influenced by undercooling effects arising from *superliquidus* pre-treatment and subsequent melt cooling to the *subliquidus* target temperature. In particular, the presence of spinifex and skeletal olive crystals in highly CaO+MgO doped samples indicate rapid growth from a poorly viscous melt (cf. Lang et al., 2021), as expected under dynamic crystallization conditions at the chilled margins of carbonate host rocks. However, these anhedral textures differ significantly from those observed for cumulus olivines growing upon sluggish undercooling/cooling conditions, whereby

euhedral habits develop during the crystallization of melts in zones near but not directly in contact with the carbonate wall-rocks (e.g.,Conte et al., 2009; Di Rocco et al., 2012; Wenzel et al., 2002).

4.2 Rheological impact of carbonate assimilation

4.2.1 Melt viscosity

From IDEs we can evaluate the rheological impact of both crystallization-driven melt compositional evolution and the physical effects of suspended crystals on viscosity evolution. For this, we extrapolate the residual melt viscosity (η_o) at 1180 °C using the MYEGA equation (Mauro et al., 2009) by combining C-DSC and F-DSC data (Table 6). The compositional changes in the melt resulting from crystallization (Fig.5) may or may not significantly impact viscosity. While the effect of CaO and CaO+MgO doping typically reduces the viscosity of the initial (crystal-free) liquid, the crystallization-driven compositional evolution of residual melts generally leads to an increase in the liquid-phase viscosity (Fig. 11). We can explore this evolution by calculating the empirical parameter *NBO/T* (i.e., the number of non-bridging oxygens *NBO* per tetrahedrally coordinated cations *T*), which is often correlated with the degree of melt polymerization (Mysen et al., 1985). At the experimental temperature of 1180 °C (i.e., within a high temperature regime of melt viscosity), the value of *NBO/T* increases as the melt viscosity decreases, outlining the depolymerizing effect of CaO and CaO+MgO addition (accompanied by a decreasing SiO_2 content) on the melt phase (see all *NBO/T* values listed in Table S1). For CaO-doped samples, the *NBO/T* shows minimal variations from the starting material C18M5 (*NBO/T* = 0.75) to the residual melts of C18M5sr1 and C18M5sr5 (*NBO/T* = 0.81 and 0.75, respectively). However, for the highly doped C26M5, the *NBO/T* decreases significantly from 1.55 in the starting material to 0.80 in the residual melt of C26M5sr1. Similarly, for CaO+MgO-doped samples, the *NBO/T* remains relatively stable in the starting material C13M8 (*NBO/T* = 0.74) and residual melts of C13M8sr1 (*NBO/T* = 0.77) and C13M8sr5 (*NBO/T*=0.74). In contrast, the highly doped sample C19M17 exhibits a notable decrease in *NBO/T,* from 1.55 in the starting material to 0.94 in the residual melt of C19M17sr1. These results indicate that significant changes in *NBO/T* occur only in the residual melts of the highly doped samples C26M5 and C19M17, corresponding to a stronger residual melt compositional evolution driven by crystallization (Fig. 5). Comparatively, Figs. 10 and S3 shows that the largest increase in viscosity occurs in C26M5sr1 and C19M17sr1 (~$10^{1.00}$ Pa·s). Nonetheless, at 1180 °C, all residual melts are characterized by a similar viscosity,

584 ranging from $10^{2.21}$ (C13M8sr5) to $10^{2.90}$ (C19M17sr1) Pa·s (Table 6). This outcome has implications for the
585 mixing efficiency of magmas when interstitial melts are extracted from the crystalline framework (Morgavi et
586 al., 2022). For instance, at the margins of a mature magma chamber in contact with carbonate host rocks, where
587 a thick solidification front develops, the formation of CaO- or CaO+MgO-rich residual melts results in near-
588 isoviscous melts, maintaining high mixing efficiency. This dynamic interaction between magmas and skarn
589 shells enhances hybridization, promoting further magma contamination and assimilation processes (Jolis et al.,
590 2013; Knuever et al., 2023a).
591
592
593
594
595
596
597
598
599
600
601
602
603
604

Figure 10. Viscosity evolution of starting and residual melts as a function of CaO and CaO+MgO addition at 1180 °C. (a) CaO-doped and (b) CaO+MgO-doped samples under shear rate of 1 s^{-1}; (c) CaO-doped and (d) CaO+MgO doped samples under shear rate of 5 s^{-1}. Circles refer to the crystal-free viscosity of the starting materials plotted against their chemical composition. Triangles and squares refer to the viscosity of the residual melts under shear rates of 1 and 5 s^{-1}, respectively, and plotted against their chemical composition. Pentagons and hexagons refer to the viscosity measured in IDEs under shear rates of 1 and 5 s^{-1}, respectively, and plotted against the residual melt composition. Dashed lines show the depolymerizing effect of CaO and CaO+MgO doping, while solid lines highlight the difference between the apparent viscosity and the viscosity of residual glass.

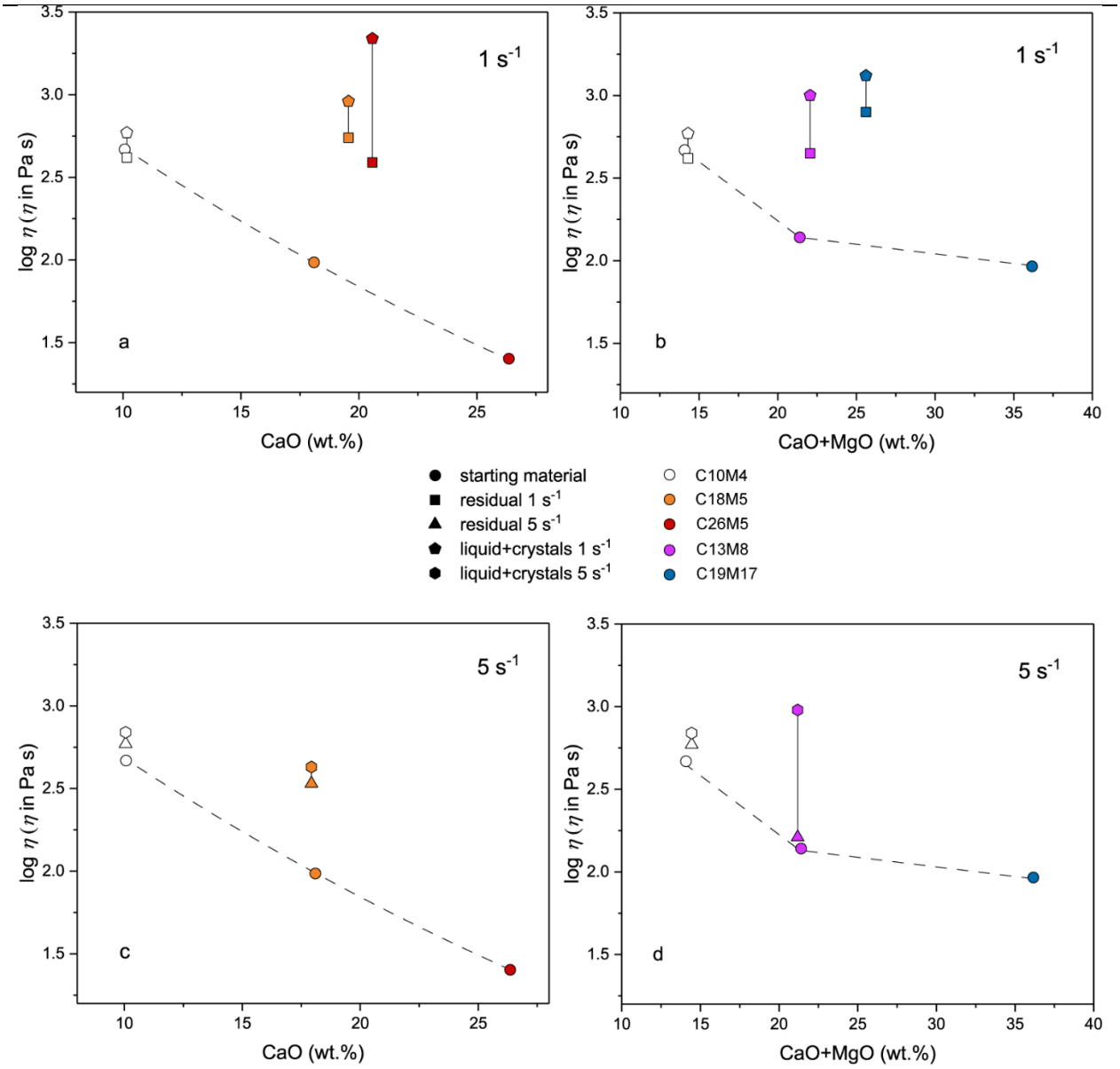

605

606 *4.2.2 Effect of crystallization*

607 To quantify the rheological changes caused by the crystallization process, we have calculated the
608 change of relative viscosity (η_r) (Table 6), which is defined as the ratio of the measured apparent viscosity of
609 the suspension (η_a) to the viscosity of the residual melt (η_o) at 1180 °C. The relative viscosity serves as a
610 measure of deviation from the behavior of a pure melt, thereby isolating the physical effect of crystallization
611 on the overall viscosity of the system (Fig. 9). The value of η_r increases from $10^{0.10}$ (C18M5sr5) to $10^{0.77}$
612 (C13M8sr5). The largest relative viscosities are calculated for samples with crystal contents of 35 and 51%
613 (C26M5sr1 and C13M8sr5), whereas the relative viscosity of other samples (C18M5sr1, C18M5sr5,
614 C13M8sr1, C18M5sr5, and C19M17sr1) is lower or, in some cases, within the uncertainties of the

615 measurements. For these samples, the apparent viscosity of the suspension closely resembles the viscosity of
616 the residual melt at lower crystal fractions. The effect of crystallinity on η_r is also compared to the viscosity
617 (η_{rm}) predicted by model of Frontoni et al. (2022), for mean aspect ratios R_m comprised between 1.9 and 4.5,
618 consistent with the variability observed in the experimental samples (Tab. 3). This model is calibrated
619 using a large database of rheological measurements, which includes natural magmas, synthetic melts, and
620 analog materials, with measurements spanning a wide range of crystal contents (1–80%) and strain rates (10^{-7}
621 to 10^{2} s^{-1}). The model builds upon a previous study by Costa et al. (2009) but includes improvements based on
622 new data to account for particle shapes and strain rate effects. Furthermore, the model of Frontoni et al. (2022)
623 considers different regimes of particle interactions, from diluted (non-interacting particles) to concentrated and
624 hyper-concentrated regimes, where particle interactions strongly influence the predicted viscosity. The input
625 parameters are the total crystallinity (Φ_{tot}) and the mean aspect ratio (R_m), (Table 3), and the shear rate ($\dot{\gamma}$). The
626 apparent viscosity (η_{am}) of the crystal-bearing suspension is determined as:

627 $$\eta_{am} = \eta_o \times \eta_{rm} \quad \text{Eq. (3)}$$

628 Results from calculations for η_{rm} and η_{am} are reported in Table 6 and illustrated in Figs. 6, 7 and 11. The
629 modeled value of η_{rm} increases from $10^{0.31}$ (C10M4sr1) to $10^{5.25}$ (C26M5sr1). As expected, the modeled values
630 increase with increasing crystal elongation (Vona et al., 2011, Mader et al., 2013). The discrepancy between
631 the modeled and measured viscosity values is quantified through the parameter $\Delta\eta_r$ (Table 6), defined as the
632 difference between η_{rm} and η_r. The model of Frontoni et al. (2022) overestimates the relative viscosity, so that
633 η_{rm} is higher than η_r (Fig. 11), with $\Delta\eta_r$ ranging from $10^{0.18}$ (C10M4sr1) to $10^{4.50}$ (C26M5sr1) Pa·s. The only
634 exception is found for sample C13M8sr5, where η_r is slightly higher than η_{rm}, resulting in a negative $\Delta\eta_r$
635 corresponding to -0.04. As a consequence, the modeled apparent viscosity η_{am} is systematically higher than
636 the stable apparent viscosity η_a measured during the IDEs (Table 4). To explain the deviation between
637 measured and modeled viscosity (η_r vs. η_{rm} or η_a vs. η_{am}), it should be noted that the model of Frontoni et al.
638 (2022) was developed accounting for only pure viscous flow regimes. For diluted and semi-diluted regimes,
639 the concentration of crystals is low, particle interactions are minimal, and the fluid behaves almost like a
640 Newtonian fluid, with a relatively small increase in viscosity as the crystal content slightly increases. In
641 contrast, for concentrated and hyper-concentrated regimes, where the crystal content is extremely high, the

642 particle interaction becomes dominant, leading to a non-Newtonian behavior. Therefore, the viscosity becomes
643 more sensitive to the strain rate and the flow exhibits more complex behaviors, such as shear thinning (Fig.
644 11). However, crystal-bearing viscosity models, such as the one proposed by Frontoni et al. (2022), do not
645 consider the effect of shear localization and departure from pure viscous behavior.
646
647 *4.2.3 Deformation regimes*
648 The rheological evolution of melts from IDEs shows two distinct deformation regimes. The viscosity
649 evolution of undoped samples (C10M4sr1 and C10M4sr5) exhibits viscous deformation, indicating a uniform
650 and continuous flow (Figs. 6a, 7a and 8b). In contrast, the viscosity of CaO- (C18M5sr1, C18M5sr5 and
651 C26M5sr1) and CaO+MgO- (C13M8sr1, C13M8sr5 and C19M17sr1) doped samples corresponds to a non-
652 homogeneous deformation (Figs. 6b-e, 7b-c and 8c), accounting for viscosity and stress drops induced by shear
653 localization and viscous/brittle rupture (Caricchi et al., 2008; Cordonnier et al., 2012; Di Fiore et al., 2021b;
654 Picard et al., 2013; Vetere et al., 2024). Note that the time required to reach rupture (t_{peak}) decreases with
655 increasing the amounts of both CaO and CaO+MgO doping levels (Table 4), as well with increasing shear rate
656 (Di Fiore et al., 2021b). Once the crystal network develops, it significantly hinders viscous flow, shifting the
657 rheology towards strain rate dependence and non-Newtonian behavior. The mechanical heterogeneities
658 introduced by the crystals compromise the structural integrity of the melt, causing stress localization and the
659 formation of shear bands, which may lead to premature rupture. For example, in sample C26M5sr1 (Fig. 2),
660 the sudden formation of a complex melilite-nepheline crystal networks results in an abrupt increase in apparent
661 viscosity ($10^{4.33}$ Pa·s), ultimately causing early brittle rupture (t_{peak} =1 hour; Figs. 6c and Table 4). A similar
662 behavior is observed in CaO+MgO doped samples C13M8sr1, C13M8sr5, and C19M17sr1 which exhibit
663 comparable crystal fractions of 30%, 35%, and 29%, respectively. In these samples, the intricate texture of the
664 mineral assemblage facilitates viscous rupture. Notably, the peak time (τ_{time} in Table 4) decreases from 5 to 4
665 h and from 5 to 3 h as the shear rate (for the same chemical composition) and CaO+MgO doping level (under
666 the same deformation regime) increase, respectively.
667 In general, for doped samples, we observe a viscous-brittle transition characterized by a drop in
668 viscosity, associated with a mean shear stress ranging from $10^{2.94}$ to $10^{4.33}$ Pa, with an average of $10^{3.59 \pm 0.53}$ Pa.
669 This transition reflects intense strain localization and material failure, with macroscopic viscous flow

potentially punctuated by localized discontinuous brittle behavior (Cordonnier et al., 2012, 2009; Lejeune and Richet, 1995). Further evidence of non-homogeneous deformation during IDEs includes strain weakening (i.e., samples C26M5sr1 and C13M8sr1) and strain hardening (i.e., samples C18M5sr1, C18M5sr5, C13M8sr5 and C19M17sr1), which are associated with crystal rearrangements following the peak and drop in apparent viscosity. As these rearrangements occur, the ability of crystals to either impede or facilitate melt flow may alternatively decrease or increase, thereby controlling the passage of the melt through the crystal network (Deubelbeiss et al., 2011; Morgan and Boettcher, 1999).

The apparent narrow variation of peak shear stress values (where the difference between the smallest and largest values corresponds to a factor of ~25), representing the mechanical strength of the investigated material, remains challenging to explain based on our experiments. Our current understanding of the shear strength of magmatic suspensions is limited, as most available studies focus on experiments conducted at relatively low temperatures and high viscosities (e.g., Cordonnier et al., 2012; Lavallée and Kendrick, 2022). At high temperatures, Di Fiore et al. (2021b) reports peak stress values in the range of $10^{4.72}$-$10^{5.28}$ Pa for experiments conducted at constant cooling rates between 1 and 10 °C/min and constant strain rates between 2.5 and 20 s^{-1}, using the same undoped phonotephritic melt investigated here. These peak stress values are approximately 1–1.5 orders of magnitude higher than those observed in our experiments for doped samples showing peak drops. Similarly to our findings, Di Fiore et al. (2021b) observed no peak stresses in isothermal crystallization experiments on the undoped phonotephritic melt conducted at temperatures between 1167 °C and 1189 °C and shear rates between 1 and 3 s^{-1}.

The mechanical strength of the material is primarily influenced by the composition of the residual liquid, the content and morphology of the crystals (which control the suspension viscosity), and the shear rate. In our experiments, no clear relationship between peak shear stress and shear rate was observed, likely due to the relatively small range of strain rates tested (1–5 s^{-1}) (Fig. S4a). Additionally, the viscosity of the residual liquid remains relatively constant (Fig. S4b), suggesting it does not significantly influence the observed variation in shear stress. Instead, crystal content generally increases with higher doping levels and shear rates (Fig.4 and Fig. S4c), while the mineral assemblage and average crystal morphology vary substantially depending on the initial melt composition and stirring conditions (Fig. S4d). Unfortunately, due to the limitations of our experimental setup, we could only analyze the mineral assemblage, crystal content and

morphology at the end of each experiment, leaving the textures present at the onset of viscous rupture unknown. The interaction of these parameters in producing different, yet comparable, rupture thresholds across experiments remains an open question that warrants further exploration.

Notably, despite both spatial heterogeneity and localized deformation are observed, all the samples exhibit an almost comparable apparent viscosity of $10^{2.63\text{-}3.34}$ Pa·s at the end of IDEs (Table 4), irrespective of their starting composition, chemical evolution, crystal content, and deformation regime. Specifically, samples subjected to a shear rate of 1 s^{-1} display a viscosity of $10^{2.77\text{-}3.34}$ Pa·s, while those subjected to a shear rate of 5 s^{-1} display a viscosity of $10^{2.63\text{-}2.98}$ Pa·s. In terms of chemical composition, CaO-doped samples exhibit a viscosity of log $10^{2.63\text{-}3.34}$ Pa·s, while CaO+MgO-doped samples exhibit a viscosity of log $10^{2.98\text{-}3.12}$ Pa·s. The undoped samples C10M4sr1 and C10M4sr5 also show similar viscosity values. This viscosity range is narrower than that expected for suspensions undergoing a pure viscous behavior, as outlined by the comparison with results from the model of Frontoni et al. (2022). For example, the sample C26M5sr1 exhibits an apparent viscosity of $10^{3.34}$ Pa·s, which is 4.5 log units lower than that predicted by model of Frontoni et al. (2022). This suggests that the complex rheological behavior attained by carbonate assimilation, including the onset of shear localization and fracturing, may reduce the resistance to flow for the doped, crystal-rich samples under the applied stress condition.

Figure 11. Variation of relative viscosity as a function of crystal fraction. The parameters η_r and η_{rm} refer to the relative viscosity calculated and modeled for IDEs using model of Frontoni et al. (2022) by considering the crystal aspect ratio, crystal fraction, and shear rate. Light and dark grey bands represent the relative viscosity-crystal fraction relationship for solid suspensions, according to the model of Frontoni et al. (2022) for aspect ratio (R_m) between 1.9 and 4.5 (Tab. 3).

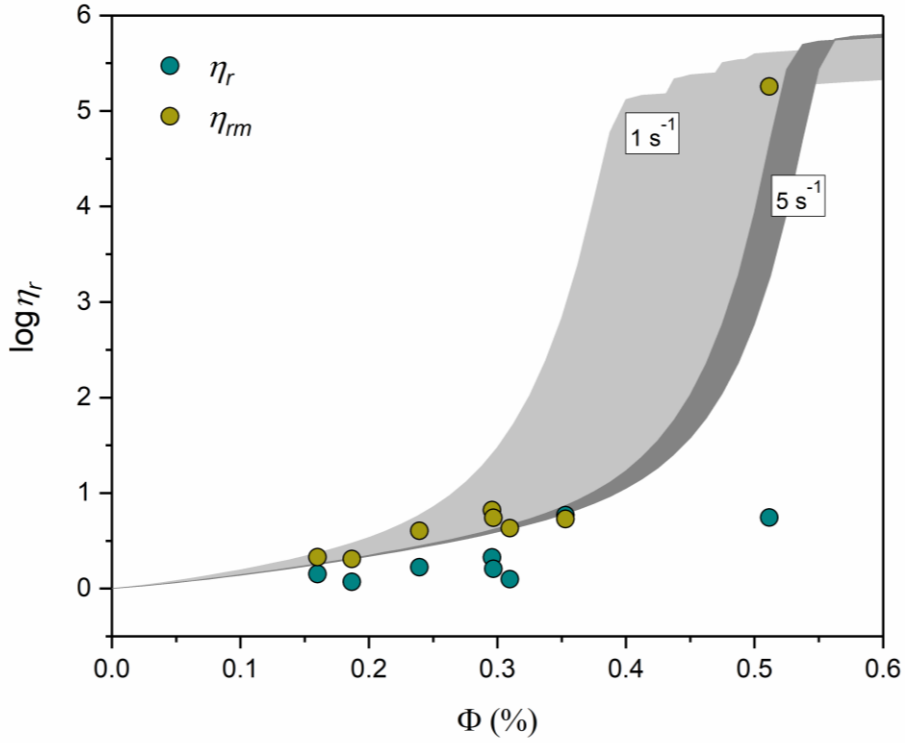

4.2.4 Implication for natural systems

Our experimental findings have significant implications for the rheological behavior of the outer portions of magma chambers emplaced within carbonate host rock, where endoskarn formation occurs (Buono et al., 2020; Colucci et al., 2024; Di Rocco et al., 2012; Di Stefano et al., 2019, 2018; Freda et al., 2011, 2008; Gaeta et al., 2009; Iacono Marziano et al., 2008; Jolis et al., 2015; Knuever et al., 2023b; Mollo et al., 2013, 2010). These crustal regions are characterized by physical deformations, decarbonation reactions, and thermal gradients that control the compositional and rheological evolution of magmas (Gudmundsson, 2012; Marsh, 2015, 2007). Strain deformation regimes, operating at the margins of magma chambers, may promote the formation of disaggregated blocks from a highly anisotropic host rock due to cracking and channelized magma flow (Paterson et al., 2012). In this context, processes such as 'skarn recycling' and 'stoping' occur, involving the detachment and subsequent assimilation of skarn fragments or carbonate wall rocks by magma (Buono et al., 2020; Gudmundsson, 2012; Jolis et al., 2015; Paterson et al., 2012, 2008). In mature magma chambers, a thick skarn shell can act as a physical barrier, inhibiting direct magma-carbonate interaction (Buono et al., 2020; Carter and Dasgupta, 2015; Jolis et al., 2015; Pappalardo et al., 2018). However, the detachment of outer

margin blocks may develop fresh contact surfaces between the magma and the carbonate host rock, thereby facilitating further contamination reactions (Jolis et al., 2015; Knuever et al., 2023b). Such detachment can be triggered by volcanic unrest, earthquakes, tremors, magma migration and pulses, thermal cracking, diking, and deformation within anisotropic wall rock (Carter and Dasgupta, 2016; Deegan et al., 2011). Therefore, the new data set provided in this experimental study enables the tracking of the rheological behavior along an idealized profile, starting from the pristine phonotephritic melt and extending towards the solidification front in contact with the carbonate host rock. In this framework, the CaO- and CaO-MgO-doped melts mimic natural hybrid magmas that have undergone variable degrees of carbonate (calcite to dolomite) assimilation at different distance from the carbonate host. Although our experiments were performed under dry conditions, atmospheric pressure, and air oxygen fugacity due to the technical limitations of the concentric cylinder apparatus, we propose that the complex rheology observed in the contaminated melts during IDEs (Figs. 5 and 6) may reflect the processes driving block detachment and skarn recycling. Ultimately, these processes are favored by the extensive crystallization of CaO- and CaO+MgO-rich melts, which are more inclined to viscous rupture and brittle behavior than uncontaminated magmas.

5. Conclusions

By integrating results from isothermal deformation experiments (IDEs) and isothermal static experiments (ISEs), we have quantified the combined effects of carbonate assimilation and shear rate on crystallization kinetics and the rheological evolution of a pristine phonotephritic melt. Relying on these experimental data, the following conclusions can be drawn:

1. the textural analysis of different phase assemblages obtained under dynamic conditions, coupled with variable CaO and CaO+MgO doping levels, lead to the formation of an intricate mineral framework due to a more effective crystallization processes, which is concurrently enhanced by chemical doping and shear rate;
2. residual melts from undoped, low CaO-doped, and low CaO+MgO-doped samples resemble the compositions of juvenile materials erupted at Somma-Vesuvius. In contrast, residual melts from high CaO-doped and high CaO+MgO-doped samples closely align with those found in skarn xenoliths;

3. using a novel approach, based on conventional and flash calorimetry, it is possible to directly estimate the viscosity of residual melts in the low-temperature regime (and viscosity range from 10^6 to 10^{12} Pa s). This approach provides a more reliable assessment of the role played by different crystallization regimes in controlling the rheological properties of the melt, compared to chemical-based models and viscosity measurements of experimentally-derived residual liquids;
4. two distinct rheological behaviors are outlined by IDEs: 1) viscous deformation, which indicates a uniform and continuous flow, and 2) non-homogeneous deformation, characterized by viscosity and stress drops due to shear localization and viscous/brittle rupture. An increase in both shear rate and carbonate assimilation favors the development of a crystal network, which significantly changes the melt rheological properties. This effect is particularly evident by the establishment of a non-Newtonian behavior, where the presence of crystals introduces mechanical heterogeneities that disrupt the uniform flow of the melt, leading to localized stress and premature crack formation.
5. the discrepancy between modeled and measured viscosities points out that modeling results do not fully capture the complexities introduced by localized deformations;
6. the apparent viscosity range documented by IDEs is much narrower than the viscosity range expected for a pure viscous behavior, as predicted by recent models. Thus, the resulting rheological behavior, characterized by shear localization and fracturing, reduces the flow resistance of the doped, crystal-rich samples under stress conditions;
7. the complex rheology observed for CaO- and CaO+MgO-doped melts, which mimic varying degrees of carbonate assimilation by magmas, likely reflects the disaggregation of skarn shells into single blocks at the periphery of the magma chambers, thereby favoring skarn recycling and magma contamination. Extensive crystallization in these skarn environments may lead to an increased susceptibility to viscous rupture and brittle failure.
8. Residual melts exhibit near-isoviscous behavior, which enhances magma mixing efficiency during the extraction of interstitial melts from the crystalline framework. This behavior is particularly significant at the margins of mature magma chambers in contact with carbonate host rocks, where CaO- or CaO+MgO-rich melts maintain high mixing efficiency within a solidification front.

Acknowledgements

Part of this work was supported by MUR-PRIN 2022 PROVES Project (Grant #2022N4FBAA) and Sapienza University of Rome Research Project 2023 (Grant #RG123188A5C103FB) to SM. DDG acknowledges the funding by Deutsche Forschungsgemeinschaft (DFG) project DI 2751/2–1 and the funding from the European Research Council (ERC) under the European Union's Horizon 2020 research and innovation programme (NANOVOLC, ERC Consolidator Grant–No. 101044772). DDG acknowledges the funding by Deutsche Forschungsgemeinschaft (DFG) project DI 2751/2–1 and the funding from the European Research Council (ERC) under the European Union's Horizon research and innovation programme (NANOVOLC, ERC Consolidator Grant–No. 101044772).

References

Adam, G., Gibbs, J.H., 1965. On the Temperature Dependence of Cooperative Relaxation Properties in Glass-Forming Liquids. J. Chem. Phys. 43, 139–146. https://doi.org/10.1063/1.1696442

Al-Mukadam, R., Di Genova, D., Bornhöft, H., Deubener, J., 2020. High rate calorimetry derived viscosity of oxide melts prone to crystallization. J. Non. Cryst. Solids 536. https://doi.org/10.1016/j.jnoncrysol.2020.119992

Arzilli, F., La Spina, G., Burton, M.R., Polacci, M., Le Gall, N., Hartley, M.E., Di Genova, D., Cai, B., Vo, N.T., Bamber, E.C., Nonni, S., Atwood, R., Llewellin, E.W., Brooker, R.A., Mader, H.M., Lee, P.D., 2019. Magma fragmentation in highly explosive basaltic eruptions induced by rapid crystallization. Nat. Geosci. 12, 1023–1028. https://doi.org/10.1038/s41561-019-0468-6

Arzilli, F., Polacci, M., La Spina, G., Le Gall, N., Llewellin, E.W., Brooker, R.A., Torres-Orozco, R., Di Genova, D., Neave, D.A., Hartley, M.E., Mader, H.M., Giordano, D., Atwood, R., Lee, P.D., Heidelbach, F., Burton, M.R., 2022. Dendritic crystallization in hydrous basaltic magmas controls magma mobility within the Earth's crust. Nat. Commun. 13. https://doi.org/10.1038/s41467-022-30890-8

Ayuso, R.A., Vivo, B. De, Rolandi, G., Seal, R.R., 1998. Geochemical and isotopic ž Nd – Pb – Sr – O / variations bearing on the genesis of volcanic rocks from Vesuvius , Italy.

Barnes, C.G., Prestvik, T., Sundvoll, B., Surratt, D., 2005. Pervasive assimilation of carbonate and silicate rocks in the Hortavær igneous complex, north-central Norway. Lithos 80, 179–199. https://doi.org/https://doi.org/10.1016/j.lithos.2003.11.002

Bruno, P.P.G., Cippitelli, G., Rapolla, A., 1998. Seismic study of the Mesozoic carbonate basement around Mt. Somma–Vesuvius, Italy. J. Volcanol. Geotherm. Res. 84, 311–322. https://doi.org/https://doi.org/10.1016/S0377-0273(98)00023-7

Buono, G., Pappalardo, L., Harris, C., Edwards, B.R., Petrosino, P., 2020. Magmatic stoping during the caldera-forming Pomici di Base eruption (Somma-Vesuvius, Italy) as a fuel of eruption explosivity. Lithos 370–371, 105628. https://doi.org/10.1016/j.lithos.2020.105628

Campagnola, S., Vona, A., Romano, C., Giordano, G., 2016. Crystallization kinetics and rheology of leucite-bearing tephriphonolite magmas from the Colli Albani volcano (Italy). Chem. Geol. 424, 12–29.

824 https://doi.org/10.1016/j.chemgeo.2016.01.012
825 Caricchi, L., Giordano, D., Burlini, L., Ulmer, P., Romano, C., 2008. Rheological properties of magma from
826 the 1538 eruption of Monte Nuovo (Phlegrean Fields, Italy): An experimental study. Chem. Geol. 256,
827 158–171. https://doi.org/10.1016/j.chemgeo.2008.06.035
828 Caricchi, L., Townsend, M., Rivalta, E., Namiki, A., 2021. The build-up and triggers of volcanic eruptions.
829 Nat. Rev. Earth Environ. https://doi.org/10.1038/s43017-021-00174-8
830 Carter, L.B., Dasgupta, R., 2016. Effect of melt composition on crustal carbonate assimilation: Implications
831 for the transition from calcite consumption to skarnification and associated CO2 degassing.
832 Geochemistry Geophys. Geosystems 17, 1312–1338. https://doi.org/10.1002/2015GC006205.Received
833 Carter, L.B., Dasgupta, R., 2015. Hydrous basalt-limestone interaction at crustal conditions: Implications for
834 generation of ultracalcic melts and outflux of CO2 at volcanic arcs. Earth Planet. Sci. Lett. 427, 202–
835 214. https://doi.org/10.1016/j.epsl.2015.06.053
836 Cassetta, M., Di Genova, D., Zanatta, M., Boffa Ballaran, T., Kurnosov, A., Giarola, M., Mariotto, G., 2021.
837 Estimating the viscosity of volcanic melts from the vibrational properties of their parental glasses. Sci.
838 Rep. 11. https://doi.org/10.1038/s41598-021-92407-5
839 Chevrel, M.O., Cimarelli, C., DeBiasi, L., Hanson, J.B., Lavallée, Y., Arzilli, F., Dingwell, D.B., 2015.
840 Viscosity measurements of crystallizing andesite from Tungurahua volcano (Ecuador). Geochemistry,
841 Geophys. Geosystems 16, 870–889. https://doi.org/10.1002/2014GC005661
842 Cioni, R., Civetta, L., Marianelli, P., METRICH, N., Santacroce, R., Sbrana, A., 1995. Compositional
843 Layering and Syn-eruptive Mixing of a Periodically Refilled Shallow Magma Chamber: the AD 79
844 Plinian Eruption of Vesuvius. J. Petrol. 36, 739–776. https://doi.org/10.1093/petrology/36.3.739
845 Civetta, L., Galati, R., Santacroce, R., 1991. Magma mixing and convective compositional layering within
846 the Vesuvius magma chamber 287–300.
847 Colucci, S., Brogi, F., Sottili, G., Montagna, C.P., Papale, P., 2024. Short-term magma-carbonate interaction:
848 A modelling perspective. Earth Planet. Sci. Lett. 628. https://doi.org/10.1016/j.epsl.2024.118592
849 Conte, A., Dolfi, D., Gaeta, M., Misiti, V., Mollo, S., Perinelli, C., Maria Dolfi, D., 2009. Experimental
850 constraints on evolution of leucite-basanite magma at 1 and 10−4 GPa: implications for parental
851 compositions of Roman high-potassium magmas. Eur. J. Mineral. 21, 763–782.

852 https://doi.org/10.1127/0935-1221/2009/0021-1934
853 Cordonnier, B., Caricchi, L., Pistone, M., Castro, J.M., Hess, K.U., Gottschaller, S., Manga, M., Dingwell,
854 D.B., Burlini, L., 2012. The viscous-brittle transition of crystal-bearing silicic melt: Direct observation
855 of magma rupture and healing. Geology 40, 611–614. https://doi.org/10.1130/G3914.1
856 Cordonnier, B., Hess, K.U., Lavallée, Y., Dingwell, D.B., 2009. Rheological properties of dome lavas: Case
857 study of Unzen volcano. Earth Planet. Sci. Lett. 279, 263–272.
858 https://doi.org/10.1016/j.epsl.2009.01.014
859 Costa, A., Caricchi, L., Bagdassarov, N.S., 2009. A model for the rheology of particle-bearing suspensions
860 and partially molten rocks. Geochemistry, Geophys. Geosystems 10.
861 https://doi.org/10.1029/2008GC002138
862 Deegan, F.M., Troll, V.R., Freda, C., Misiti, V., Chadwick, J.P., 2011. Fast and furious: crustal CO2 release
863 at Merapi volcano, Indonesia. Geol. Today 27, 63–64. https://doi.org/https://doi.org/10.1111/j.1365-
864 2451.2011.00785.x
865 Del Gaudio, P., Ventura, G., 2008. Mechanical erosion of xenoliths by magmatic shear flow. Geophys. Res.
866 Lett. 35, 1–5. https://doi.org/10.1029/2008GL033781
867 Del Moro, A., Fulignati, P., Marianelli, P., Sbrana, A., 2001. Magma contamination by direct wall rock
868 interaction: constraints from xenoliths from the walls of a carbonate-hosted magma chamber (Vesuvius
869 1944 eruption).
870 Deubelbeiss, Y., Kaus, B.J.P., Connolly, J.A.D., Caricchi, L., 2011. Potential causes for the non-Newtonian
871 rheology of crystal-bearing magmas. Geochemistry, Geophys. Geosystems 12, 1–22.
872 https://doi.org/10.1029/2010GC003485
873 Di Fiore, F., Mollo, S., Vona, A., MacDonald, A., Ubide, T., Nazzari, M., Romano, C., Scarlato, P., 2021a.
874 Kinetic partitioning of major and trace cations between clinopyroxene and phonotephritic melt under
875 convective stirring conditions: New insights into clinopyroxene sector zoning and concentric zoning.
876 Chem. Geol. 584. https://doi.org/10.1016/j.chemgeo.2021.120531
877 Di Fiore, F., Vona, A., Costa, A., Mollo, S., Romano, C., 2022. Quantifying the influence of cooling and
878 shear rate on the disequilibrium rheology of a trachybasaltic melt from Mt . Etna. Earth Planet. Sci.
879 Lett. 594, 117725. https://doi.org/10.1016/j.epsl.2022.117725

Di Fiore, F., Vona, A., Di Genova, D., Pontesilli, A., Calabrò, L., Mollo, S., Taddeucci, J., Romano, C., Scarlato, P., 2024. Magma titanium and iron contents dictate crystallization timescales and rheological behaviour in basaltic volcanic systems. Commun. Earth Environ. 5. https://doi.org/10.1038/s43247-024-01452-1

Di Fiore, F., Vona, A., Kolzenburg, S., Mollo, S., Romano, C., 2021b. An Extended Rheological Map of Pāhoehoe—'A'ā Transition. J. Geophys. Res. Solid Earth 126. https://doi.org/10.1029/2021JB022035

Di Fiore, F., Vona, A., Mollo, S., Nazzari, M., Giordano, G., Romano, C., 2023. Experimental insights on the shear-induced crystallization of a phonotephrite magma. Chem. Geol. 637. https://doi.org/10.1016/j.chemgeo.2023.121682

Di Genova, D., Bondar, D., Zandonà, A., Valdivia, P., Al-Mukadam, R., Fei, H., Withers, A.C., Boffa Ballaran, T., Kurnosov, A., McCammon, C., Deubener, J., Katsura, T., 2023. Viscosity of anhydrous and hydrous peridotite melts. Chem. Geol. 625. https://doi.org/10.1016/j.chemgeo.2023.121440

Di Genova, D., Brooker, R.A., Mader, H.M., Drewitt, J.W.E., Longo, A., Deubener, J., Neuville, D.R., Fanara, S., Shebanova, O., Anzellini, S., Arzilli, F., Bamber, E.C., Hennet, L., Spina, G. La, Miyajima, N., 2020a. In situ observation of nanolite growth in volcanic melt: A driving force for explosive eruptions. Sci. Adv. 6, eabb0413. https://doi.org/10.1126/sciadv.abb0413

Di Genova, D., Zandonà, A., Deubener, J., 2020b. Unravelling the effect of nano-heterogeneity on the viscosity of silicate melts: Implications for glass manufacturing and volcanic eruptions. J. Non. Cryst. Solids 545. https://doi.org/10.1016/j.jnoncrysol.2020.120248

Di Rocco, T., Freda, C., Gaeta, M., Mollo, S., Dallai, L., 2012. Magma chambers emplaced in carbonate substrate: Petrogenesis of skarn and cumulate rocks and implications for CO 2 degassing in volcanic areas. J. Petrol. 53, 2307–2332. https://doi.org/10.1093/petrology/egs051

Di Stefano, F., Mollo, S., Blundy, J.D., Scarlato, P., Nazzari, M., Bachmann, O., 2019. The effect of CaO on the partitioning behavior of REE, Y and Sc between olivine and melt: Implications for basalt-carbonate interaction processes. Lithos 326–327, 327–340. https://doi.org/10.1016/j.lithos.2018.12.019

Di Stefano, F., Mollo, S., Scarlato, P., Nazzari, M., Bachmann, O., Caruso, M., 2018. Olivine compositional changes in primitive magmatic skarn environments: A reassessment of divalent cation partitioning models to quantify the effect of carbonate assimilation. Lithos 316–317, 104–121.

908 https://doi.org/10.1016/j.lithos.2018.07.008
909 Fanesi, E., Di Genova, D., Valdivia, P., Bondar, D., Dominijanni, S., S., A., Giuliani, G., Giordano, G.,
910 Cassetta, M., Vona, A., Romano, C., Arzilli, F., 2025. A review of the Differential Scanning
911 Calorimetry shift–factor approach: Application to Colli Albani melt viscosity and implications for
912 mafic Plinian eruptions. J. Volcanol. Geotherm. Res. 134226.
913 https://doi.org/10.1016/j.jvolgeores.2025.108276
914 Freda, C., Gaeta, M., Giaccio, B., Marra, F., Palladino, D.M., Scarlato, P., Sottili, G., 2011. CO2-driven
915 large mafic explosive eruptions: The Pozzolane Rosse case study from the Colli Albani Volcanic
916 District (Italy). Bull. Volcanol. 73, 241–256. https://doi.org/10.1007/s00445-010-0406-3
917 Freda, C., Gaeta, M., Misiti, V., Mollo, S., Dolfi, D., Scarlato, P., 2008. Magma-carbonate interaction: An
918 experimental study on ultrapotassic rocks from Alban Hills (Central Italy). Lithos 101, 397–415.
919 https://doi.org/10.1016/j.lithos.2007.08.008
920 Frontoni, A., Costa, A., Vona, A., Romano, C., 2022. A comprehensive database of crystal-bearing magmas
921 for the calibration of a rheological model. Sci. Data 9, 1–11. https://doi.org/10.1038/s41597-022-
922 01363-w
923 Fulignati, P., Marianelli, P., Santacroce, R., Sbrana, A., 2004. Probing the Vesuvius magma chamber-host
924 rock interface through xenoliths. Geol. Mag. 141, 417–428.
925 https://doi.org/10.1017/S0016756804009392
926 Fulignati, P., Marianelli, P., Santacroce, R., Sbrana, A., 2000. The skarn shell of the 1944 Vesuvius magma
927 chamber. Genesis and P-T-X conditions from melt and fluid inclusion data. Eur. J. Mineral. 12, 1025–
928 1039. https://doi.org/10.1127/0935-1221/2000/0012-1025
929 Gaeta, M., Di Rocco, T., Freda, C., 2009. Carbonate assimilation in open magmatic systems: The role of
930 melt-bearing skarns and cumulate-forming processes. J. Petrol. 50, 361–385.
931 https://doi.org/10.1093/petrology/egp002
932 Gaeta, M., Fabrizio, G., Cavarretta, G., 2000. F-phlogopites in the Alban Hills Volcanic District (Central
933 Italy): Indications regarding the role of volatiles in magmatic crystallisation. J. Volcanol. Geotherm.
934 Res. 99, 179–193. https://doi.org/10.1016/S0377-0273(00)00172-4
935 Gilg, H.A., Lima, A., Somma, R.Y., Belkin, H.E., De Vivo, B., Ayuso, R.A., 2001. Isotope geochemistry

and fluid inclusion study of skarns from Vesuvius. Mineral. Petrol. 73, 145–176.

Giordano, D., Russell, J.K., Dingwell, D.B., 2008. Viscosity of magmatic liquids: A model. Earth Planet. Sci. Lett. 271, 123–134. https://doi.org/10.1016/j.epsl.2008.03.038

Giuliani, G., Di Genova, D., Di Fiore, F., Valdivia, P., Mollo, S., Romano, C., Boffa Ballaran, T., Kurnosov, A., Vona, A., 2024. The effect of carbonate assimilation and nanoheterogeneities on the viscosity of phonotephritic melt from Vesuvius. Chem. Geol. 670, 122408. https://doi.org/10.1016/j.chemgeo.2024.122408

Gottsmann, J., Giordano, D., Dingwell, D.B., 2002. Predicting shear viscosity during volcanic processes at the glass transition: a calorimetric calibration. Earth Planet. Sci. Lett. 198, 417–427. https://doi.org/https://doi.org/10.1016/S0012-821X(02)00522-8

Gudmundsson, A., 2012. Magma chambers: Formation, local stresses, excess pressures, and compartments. J. Volcanol. Geotherm. Res. 237–238, 19–41. https://doi.org/10.1016/j.jvolgeores.2012.05.015

Hammer, J., 2008. Experimental Studies of the Kinetics and Energetics of Magma Crystallization. Rev. Mineral. Geochemistry 69, 9–59. https://doi.org/10.2138/rmg.2008.69.2

Harris, A., Mannini, S., Thivet, S., Chevrel, M.O., Gurioli, L., 2020. How shear helps lava to flow. Geology 48. https://doi.org/10.1130/G47110.1ï

Harris, M.A., Chevrel, M.O., Parsons, J.T., Latchimy, T., Thordarson, T., Höskuldsson, A., Moreland, W.M., Payet–Clerc, M., Kolzenburg, S., 2024. Real-time, in situ viscosity mapping of active lava. Geology 53, 181–185. https://doi.org/10.1130/G52558.1

Hui, H., Zhang, Y., 2007. Toward a general viscosity equation for natural anhydrous and hydrous silicate melts. Geochim. Cosmochim. Acta 71, 403–416. https://doi.org/10.1016/j.gca.2006.09.003

Iacono Marziano, G., Gaillard, F., Pichavant, M., 2008. Limestone assimilation by basaltic magmas: An experimental re-assessment and application to Italian volcanoes. Contrib. to Mineral. Petrol. 155, 719–738. https://doi.org/10.1007/s00410-007-0267-8

Iacono Marziano, G., Gaillard, F., Pichavant, M., 2007. Limestone assimilation and the origin of CO2 emissions at the Alban Hills (Central Italy): Constraints from experimental petrology. J. Volcanol. Geotherm. Res. 166, 91–105. https://doi.org/10.1016/j.jvolgeores.2007.07.001

Jolis, E.M., Freda, C., Troll, V.R., Deegan, F.M., Blythe, L.S., McLeod, C.L., Davidson, J.P., 2013.

964 Experimental simulation of magma-carbonate interaction beneath Mt. Vesuvius, Italy. Contrib. to
965 Mineral. Petrol. 166, 1335–1353. https://doi.org/10.1007/s00410-013-0931-0
966 Jolis, E.M., Troll, V.R., Harris, C., Freda, C., Gaeta, M., Orsi, G., Siebe, C., 2015. Skarn xenolith record
967 crustal CO2 liberation during Pompeii and Pollena eruptions, Vesuvius volcanic system, central Italy.
968 Chem. Geol. 415, 17–36. https://doi.org/10.1016/j.chemgeo.2015.09.003
969 Knuever, M., Mele, D., Sulpizio, R., 2023a. Mineralization and Skarn Formation Associated with Alkaline
970 Magma Chambers Emplaced in a Limestone Basement: A Review. Minerals.
971 https://doi.org/10.3390/min13091184
972 Knuever, M., Sulpizio, R., Mele, D., Costa, A., 2023b. Magma–rock interactions: a review of their influence
973 on magma rising processes with emphasis on short-timescale assimilation of carbonate rocks. Geol.
974 Soc. London, Spec. Publ. 520, 101–120. https://doi.org/10.1144/sp520-2021-177
975 Kolzenburg, S., Chevrel, M.O., Dingwell, D.B., 2022. Magma / Suspension Rheology. Rev. Mineral.
976 Geochemistry 87, 639–720. https://doi.org/10.2138/rmg.2022.87.14
977 Kolzenburg, S., Giordano, D., Cimarelli, C., Dingwell, D.B., 2016. In situ thermal characterization of
978 cooling/crystallizing lavas during rheology measurements and implications for lava flow emplacement.
979 Geochim. Cosmochim. Acta 195, 244–258. https://doi.org/10.1016/j.gca.2016.09.022
980 Kolzenburg, S., Giordano, D., Hess, K.U., Dingwell, D.B., 2018. Shear Rate-Dependent Disequilibrium
981 Rheology and Dynamics of Basalt Solidification. Geophys. Res. Lett. 45, 6466–6475.
982 https://doi.org/10.1029/2018GL077799
983 Kolzenburg, S., Hess, K.U., Berlo, K., Dingwell, D.B., 2020. Disequilibrium Rheology and Crystallization
984 Kinetics of Basalts and Implications for the Phlegrean Volcanic District. Front. Earth Sci. 8.
985 https://doi.org/10.3389/feart.2020.00187
986 Kouchi, A., Tsuchiyama, A., Sunagawa, I., 1986. Contributions to Mineralogy and Petrology Effect of
987 stirring on crystallization kinetics of basalt: texture and element partitioning, Contrib Mineral Petrol.
988 Lang, S., Mollo, S., France, L., Misiti, V., Nazzari, M., 2021. Kinetic partitioning of major-minor cations
989 between olivine and Hawaiian tholeiitic basalt under variable undercooling and cooling rate conditions.
990 Chem. Geol. 584. https://doi.org/10.1016/j.chemgeo.2021.120485
991 Langhammer, D., Di Genova, D., Steinle-Neumann, G., 2022. Modeling Viscosity of Volcanic Melts With

992 Artificial Neural Networks. Geochemistry, Geophys. Geosystems 23.
993 https://doi.org/10.1029/2022GC010673
994 Langhammer, D., Di Genova, D., Steinle-Neumann, G., 2021. Modeling the Viscosity of Anhydrous and
995 Hydrous Volcanic Melts. Geochemistry, Geophys. Geosystems 22.
996 https://doi.org/10.1029/2021GC009918
997 Lavallée, Y., Kendrick, J.E., 2022. Strain Localization in Magmas. Rev. Mineral. Geochemistry 87, 721–
998 765. https://doi.org/10.2138/rmg.2022.87.15
999 Le Bas, M.J., MAITRE, R.W.L.E., STRECKEISEN, A., ZANETTIN, B., 1986. A Chemical Classification
1000 of Volcanic Rocks Based on the Total Alkali-Silica Diagram. J. Petrol. 27, 745–750.
1001 https://doi.org/10.1093/petrology/27.3.745
1002 Lejeune, A.M., Richet, P., 1995. Rheology of crystal-bearing silicate melts: an experimental study at high
1003 viscosities. J. Geophys. Res. 100, 4215–4229. https://doi.org/10.1029/94JB02985
1004 Lustrino, M., Luciani, N., Stagno, V., Narzisi, S., Masotta, M., Scarlato, P., 2022. Experimental evidence on
1005 the origin of Ca-rich carbonated melts formed by interaction between sedimentary limestones and
1006 mantle-derived ultrabasic magmas. Geology 50, 476–480. https://doi.org/10.1130/G49621.1
1007 Macdonald, R., Bagiński, B., Rolandi, G., De Vivo, B., Kopczyńska, A., 2016. Petrology of parasitic and
1008 eccentric cones on the flanks and base of Somma-Vesuvius. Mineral. Petrol. 110, 65–85.
1009 https://doi.org/10.1007/s00710-015-0410-6
1010 Mader, H.M., Llewellin, E.W., Mueller, S.P., 2013. The rheology of two-phase magmas: A review and
1011 analysis. J. Volcanol. Geotherm. Res. https://doi.org/10.1016/j.jvolgeores.2013.02.014
1012 Marsh, B.D., 2015. Magma Chambers, Second Edi. ed, The Encyclopedia of Volcanoes. Elsevier Inc.
1013 https://doi.org/10.1016/B978-0-12-385938-9.00008-0
1014 Marsh, B.D., 2007. 6.07 - Magmatism, Magma, and Magma Chambers. Treatise Geophys. Vol. 1-10 1–10,
1015 275–333. https://doi.org/10.1016/B978-044452748-6.00106-1
1016 Mauro, J.C., Yue, Y., Ellison, A.J., Gupta, P.K., Allan, D.C., 2009. Viscosity of glass-forming liquids. Proc.
1017 Natl. Acad. Sci. 106, 19780–19784. https://doi.org/10.1073/pnas.0911705106
1018 Moitra, P., Gonnermann, H.M., 2015. Effects of crystal shape- and size-modality on magma rheology.
1019 Geochemistry, Geophys. Geosystems 16, 1–26. https://doi.org/https://doi.org/10.1002/2014GC005554

Mollo, S., Blundy, J.D., Scarlato, P., Vetere, F., Holtz, F., Bachmann, O., Gaeta, M., 2020. A review of the lattice strain and electrostatic effects on trace element partitioning between clinopyroxene and melt: Applications to magmatic systems saturated with Tschermak-rich clinopyroxenes. Earth-Science Rev. https://doi.org/10.1016/j.earscirev.2020.103351

Mollo, S., Di Fiore, F., Macdonald, A., Ubide, T., Pontesilli, A., Giuliani, G., Vona, A., Romano, C., Scarlato, P., 2024. Thermodynamics and kinetics of cation partitioning between plagioclase and trachybasaltic melt in static and dynamic systems : A reassessment of the lattice strain and electrostatic energies of substitution 384, 27–43.

Mollo, S., Gaeta, M., Freda, C., Di Rocco, T., Misiti, V., Scarlato, P., 2010. Carbonate assimilation in magmas: A reappraisal based on experimental petrology. Lithos 114, 503–514. https://doi.org/10.1016/j.lithos.2009.10.013

Mollo, S., Heap, M.J., Dingwell, D.B., Hess, K.U., Iezzi, G., Masotta, M., Scarlato, P., Vinciguerra, S., 2013. Decarbonation and thermal microcracking under magmatic P-T-fco2 conditions: The role of skarn substrata in promoting volcanic instability. Geophys. J. Int. 195, 369–380. https://doi.org/10.1093/gji/ggt265

Mollo, S., Vona, A., 2014. The geochemical evolution of clinopyroxene in the Roman Province: A window on decarbonation from wall-rocks to magma. Lithos 192–195, 1–7. https://doi.org/10.1016/j.lithos.2014.01.009

Morgan, D.J., Jerram, D.A., 2006. On estimating crystal shape for crystal size distribution analysis. J. Volcanol. Geotherm. Res. 154, 1–7. https://doi.org/10.1016/j.jvolgeores.2005.09.016

Morgan, J.K., Boettcher, M.S., 1999. Numerical simulations of granular shear zones using the distinct element method: 2. Effects of particle size distribution and interparticle friction on mechanical behavior. J. Geophys. Res. Solid Earth 104, 2721–2732. https://doi.org/10.1029/1998jb900055

Morgavi, D., Laumonier, M., Petrelli, M., Dingwell, D.B., 2022. Decrypting Magma Mixing in Igneous Systems. Rev. Mineral. Geochemistry 87, 607–638. https://doi.org/10.2138/rmg.2022.87.13

Mueller, S.P., Llewellin, E.W., Mader, H.M., 2010. The rheology of suspensions of solid particles. Proc. R. Soc. A Math. Phys. Eng. Sci. 466, 1201–1228.

Mysen, B., Virgo, D., Seifert, F.A., 1985. Relationships between properties and structure of aluminosilicate

melts. Am. Mineral. 70, 88–105.

Narayanaswamy, O.S., 1971. A Model of Structural Relaxation in Glass. J. Am. Ceram. Soc. 54, 491–498. https://doi.org/https://doi.org/10.1111/j.1151-2916.1971.tb12186.x

Pabst, W., Gregorová, E., Berthold, C., 2006. Particle shape and suspension rheology of short-fiber systems. J. Eur. Ceram. Soc. 26, 149–160. https://doi.org/10.1016/j.jeurceramsoc.2004.10.016

Pappalardo, L., Buono, G., Fanara, S., Petrosino, P., 2018. Combining textural and geochemical investigations to explore the dynamics of magma ascent during Plinian eruptions: a Somma–Vesuvius volcano (Italy) case study. Contrib. to Mineral. Petrol. 173. https://doi.org/10.1007/s00410-018-1486-x

Paterson, S.R., Memeti, V., Pignotta, G.S., Erdmann, S., Žák, J., Chambers, J., Ianno, A., 2012. Formation and transfer of stoped blocks into magma chambers: The hightemperature interplay between focused porous flow, cracking, channel flow, host-rock anisotropy, and regional deformation. Geosphere 8, 443–469. https://doi.org/10.1130/GES00680.1

Paterson, S.R., Pignotta, G.S., Farris, D., Memeti, V., Miller, R.B., Vernon, R.H., Žák, J., 2008. Is stoping a volumetrically significant pluton emplacement process?: Discussion. Bull. Geol. Soc. Am. 120, 1075–1079. https://doi.org/10.1130/B26148.1

Peccerillo, A., 2019. Campania volcanoes: Petrology, geochemistry, and geodynamic significance, Vesuvius, Campi Flegrei, and Campanian Volcanism. Elsevier Inc. https://doi.org/10.1016/B978-0-12-816454-9.00005-5

Peccerillo, A., 2001. Geochemical similarities between the Vesuvius , Phlegraean Fields and Stromboli Volcanoes : petrogenetic , geodynamic and volcanological implications 93–105.

Picard, D., Arbaret, L., Pichavant, M., Champallier, R., Launeau, P., 2013. The rheological transition in plagioclase-bearing magmas. J. Geophys. Res. Solid Earth 118, 1363–1377. https://doi.org/10.1002/jgrb.50091

Pistone, M., Cordonnier, B., Ulmer, P., Caricchi, L., 2016. Rheological flow laws for multiphase magmas: An empirical approach. J. Volcanol. Geotherm. Res. 321, 158–170. https://doi.org/10.1016/j.jvolgeores.2016.04.029

Rosi, M., Santacroce, R., 1983. The A.D. 472 “Pollena” eruption: volcanological and petrological data for this poorly-known, plinian-type event at vesuvius. J. Volcanol. Geotherm. Res. 17, 249–271.

https://doi.org/https://doi.org/10.1016/0377-0273(83)90071-9

Santacroce, R., Cioni, R., Marianelli, P., Sbrana, A., Sulpizio, R., Zanchetta, G., Donahue, D.J., Joron, J.L., 2008. Age and whole rock-glass compositions of proximal pyroclastics from the major explosive eruptions of Somma-Vesuvius: A review as a tool for distal tephrostratigraphy. J. Volcanol. Geotherm. Res. 177, 1–18. https://doi.org/10.1016/j.jvolgeores.2008.06.009

Scarani, A., Vona, A., Di Genova, D., Al-Mukadam, R., Romano, C., Deubener, J., 2022a. Determination of cooling rates of glasses over four orders of magnitude. Contrib. to Mineral. Petrol. 177. https://doi.org/10.1007/s00410-022-01899-5

Scarani, A., Zandonà, A., Di Fiore, F., Valdivia, P., Putra, R., Miyajima, N., Bornhöft, H., Vona, A., Deubener, J., Romano, C., Di Genova, D., 2022b. A chemical threshold controls nanocrystallization and degassing behaviour in basalt magmas. Commun. Earth Environ. 3, 284. https://doi.org/10.1038/s43247-022-00615-2

Scherer, G.W., 1984. Use of the Adam-Gibbs Equation in the Analysis of Structural Relaxation. J. Am. Ceram. Soc. 67, 504–511. https://doi.org/https://doi.org/10.1111/j.1151-2916.1984.tb19643.x

Scherer, G.W., n.d. Use of the Adam-Gibbs Equation in the Analysis of Structural Relaxation.

Sehlke, A., Whittington, A., 2020. Rheology of a KREEP analog magma : Experimental results applied to dike ascent through the lunar crust. Planet. Space Sci. 187, 104941. https://doi.org/10.1016/j.pss.2020.104941

Sehlke, A., Whittington, A., Robert, B., Harris, A., Gurioli, L., Médard, E., 2014. Pahoehoe to áá transition of Hawaiian lavas: An experimental study. Bull. Volcanol. 76. https://doi.org/10.1007/s00445-014-0876-9

Soldati, A., Cimarelli, C., Kueppers, U., Cáceres, F., Müller, D., Pankhurst, M., Scarrow, J.H., Perez, N., Dingwell, D.B., 2024. Melt viscosity tracks the volcanic and magmatic evolution of the 2021 Tajogaite eruption, La Palma (Canary Islands). J. Volcanol. Geotherm. Res. 455. https://doi.org/10.1016/j.jvolgeores.2024.108210

Soldati, A., Sehlke, A., Chigna, G., Whittington, A., 2016. Field and experimental constraints on the rheology of arc basaltic lavas : the January 2014 Eruption of Pacaya (Guatemala). Bull. Volcanol. https://doi.org/10.1007/s00445-016-1031-6

Somma, R.Y., Ayuso, R.A., Vivo, B. De, Rolandi, G., Napoli, Á., Ii, F., 2001. Major , trace element and isotope geochemistry (Sr-Nd-Pb) of interplinian magmas from Mt . Somma-Vesuvius (Southern Italy).

Stabile, P., Sicola, S., Giuli, G., Paris, E., Carroll, M.R., Deubener, J., Di Genova, D., 2021. The effect of iron and alkali on the nanocrystal-free viscosity of volcanic melts: A combined Raman spectroscopy and DSC study. Chem. Geol. 559. https://doi.org/10.1016/j.chemgeo.2020.119991

Stevenson, R.J., Dingwell, D.B., Webb, S.L., Bagdassarov, N.S., 1995. The equivalence of enthalpy and shear stress relaxation in rhyolitic obsidians and quantification of the liquid-glass transition in volcanic processes. J. Volcanol. Geotherm. Res. 68, 297–306. https://doi.org/10.1016/0377-0273(95)00015-1

Sulpizio, R., Mele, D., Dellino, P., La Volpe, L., 2005. A complex, Subplinian-type eruption from low-viscosity, phonolitic to tephri-phonolitic magma: The AD 472 (Pollena) eruption of Somma-Vesuvius, Italy. Bull. Volcanol. 67, 743–767. https://doi.org/10.1007/s00445-005-0414-x

Tripoli, B., Manga, M., Mayeux, J., Barnard, H., 2019. The Effects of Deformation on the Early Crystallization Kinetics of Basaltic Magmas. Front. Earth Sci. 7. https://doi.org/10.3389/feart.2019.00250

Valdivia, P., Zandonà, A., Kurnosov, A., Ballaran, T.B., Deubener, J., Di Genova, D., 2023. Are volcanic melts less viscous than we thought? The case of Stromboli basalt. Contrib. to Mineral. Petrol. 178. https://doi.org/10.1007/s00410-023-02024-w

Valdivia, P., Zandonà, A., Löschmann, J., Bondar, D., Genevois, C., Allix, M., Miyajima, N., Kurnosov, A., Boffa Ballaran, T., Di Fiore, F., Vona, A., Romano, C., Deubener, J., Bamber, E.C., Di Genova, D., 2024a. Nanoscale chemical heterogeneities control magma viscosity and failure. Under Rev. 1–25. https://doi.org/10.21203/rs.3.rs-3891365/v1

Valdivia, P., Zandonà, A., Löschmann, J., Bondar, D., Genevois, C., Allix, M., Miyajima, N., Kurnosov, A., Boffa Ballaran, T., Di Fiore, F., Vona, A., Romano, C., Deubener, J., Bamber, E.C., Di Genova, D., 2024b. Nanoscale chemical heterogeneities control magma viscosity and failure. Under Rev. 1–25. https://doi.org/https://doi.org/10.21203/rs.3.rs-3891365/v1

Vetere, F., Holtz, F., 2020. Rheological Behavior of Partly Crystallized Silicate Melts Under Variable Shear Rate, in: Dynamic Magma Evolution. American Geophysical Union (AGU), pp. 153–167.

https://doi.org/https://doi.org/10.1002/9781119521143.ch7

Vetere, F., Merseburger, S., Pisello, A., Perugini, D., Viti, C., Petrelli, M., Musu, A., Almeev, R., Caricchi, L., Iezzi, G., Cassetta, M., Holtz, F., 2024. The role of deformation on the early crystallization and rheology of basaltic liquids. Earth Planet. Sci. Lett. 644, 118934. https://doi.org/10.1016/j.epsl.2024.118934

Vetere, F., Petrelli, M., Perugini, D., Haselbach, S., Morgavi, D., Pisello, A., Iezzi, G., Holtz, F., 2021. Rheological evolution of eruptible Basaltic-Andesite Magmas under dynamic conditions: The importance of plagioclase growth rates. J. Volcanol. Geotherm. Res. 420, 107411. https://doi.org/10.1016/j.jvolgeores.2021.107411

Vona, A., Romano, C., 2013. The effects of undercooling and deformation rates on the crystallization kinetics of Stromboli and Etna basalts. Contrib. to Mineral. Petrol. 166, 491–509. https://doi.org/10.1007/s00410-013-0887-0

Vona, A., Romano, C., Dingwell, D.B., Giordano, D., 2011. The rheology of crystal-bearing basaltic magmas from Stromboli and Etna. Geochim. Cosmochim. Acta 75, 3214–3236. https://doi.org/10.1016/j.gca.2011.03.031

Vona, A., Romano, C., Giordano, G., Sulpizio, R., 2020. Linking magma texture, rheology and eruptive style during the 472 AD Pollena Subplinian eruption (Somma-Vesuvius). Lithos 370–371. https://doi.org/10.1016/j.lithos.2020.105658

Webb, S.L., Knoche, R., 1996. The glass-transition, structural relaxation and shear viscosity of silicate melts. Chem. Geol. 128, 165–183. https://doi.org/10.1016/0009-2541(95)00171-9

Wenzel, T., Baumgartner, L.P., Brugmann, G.E., Konnikov, E.G., Kislov, E. V, 2002. Partial Melting and Assimilation of Dolomitic Xenoliths by Mafic Magma: the Ioko-Dovyren Intrusion (North Baikal Region, Russia). J. Petrol. 43, 2049–2074. https://doi.org/10.1093/petrology/43.11.2049

Whitley, S., Halama, R., Gertisser, R., Preece, K., Deegan, F.M., Troll, V.R., 2020. Magmatic and metasomatic effects of magma–carbonate interaction recorded in calc-silicate xenoliths from Merapi volcano (Indonesia). J. Petrol. 61. https://doi.org/10.1093/petrology/egaa048

Yue, Y., Von der Ohe, R., Jensen, S.L., 2004. Fictive temperature, cooling rate, and viscosity of glasses. J. Chem. Phys. 120, 8053–8059. https://doi.org/10.1063/1.1689951

Yue, Y.Z., 2008. Characteristic temperatures of enthalpy relaxation in glass. J. Non. Cryst. Solids 354, 1112–1118. https://doi.org/10.1016/j.jnoncrysol.2006.11.027

Zandonà, A., Scarani, A., Löschmann, J., Cicconi, M.R., Di Fiore, F., de Ligny, D., Deubener, J., Vona, A., Allix, M., Di Genova, D., 2023. Non-stoichiometric crystal nucleation in a spodumene glass containing TiO2 as seed former: Effects on the viscosity of the residual melt. J. Non. Cryst. Solids 619, 122563. https://doi.org/https://doi.org/10.1016/j.jnoncrysol.2023.122563

Zheng, Q., Mauro, J.C., Ellison, A.J., Potuzak, M., Yue, Y., 2011. Universality of the high-temperature viscosity limit of silicate liquids. Phys. Rev. B 83, 212202. https://doi.org/10.1103/PhysRevB.83.212202